

# Kinematic properties of the field elliptical NGC 7507<sup>★,★★</sup>

R. Salinas<sup>1,2,★★★</sup>, T. Richtler<sup>1</sup>, L. P. Bassino<sup>3</sup>, A. J. Romanowsky<sup>4</sup>, and Y. Schuberth<sup>5</sup>

<sup>1</sup> Departamento de Astronomía, Universidad de Concepción, Concepción, Chile  
e-mail: rcsave@utu.fi

<sup>2</sup> European Southern Observatory, Alonso de Córdova 3107, Santiago, Chile

<sup>3</sup> Facultad de Ciencias Astronómicas y Geofísicas de la Universidad Nacional de La Plata and Instituto de Astrofísica de la Plata (CCT La Plata-CONICET-UNLP), Paseo del Bosque S/N, 1900 La Plata, Argentina

<sup>4</sup> UCO/Lick Observatory, University of California, Santa Cruz, CA 95064, USA

<sup>5</sup> Argelander Institut für Astronomie, Auf dem Hügel 71, 53121 Bonn, Germany

Received 14 January 2011 / Accepted 7 November 2011

## ABSTRACT

The dark matter (DM) halos of field elliptical galaxies have not been well-studied and their properties appear controversial in the literature. While some galaxies appear to be nearly devoid of DM, others show clear evidence of its presence. Furthermore, modified Newtonian dynamics (MOND), which has been found to have predictive power in the domain of disk galaxies, has not yet been investigated for isolated elliptical galaxies. We study the kinematics of the isolated elliptical NGC 7507, which has been claimed as a clear example of DM presence in early-type galaxies. We obtained major and minor axis long-slit spectroscopy of NGC 7507 using the Gemini South telescope and deep imaging in Kron-Cousins *R* and Washington *C* using the CTIO/MOSAIC camera. Mean velocities, velocity dispersion and higher order moments of the velocity distribution are measured out to  $\sim 90''$ . The galaxy, although almost circular, has significant rotation along the minor axis and a rapidly declining velocity dispersion along both axes. The velocity dispersion profile is modeled in the context of a spherical Jeans analysis. Models without DM provide an excellent representation of the data with a mass-to-light ratio ( $M/L$ ) of 3.1 (*R*-band). The most massive Navarro-Frenk-White (NFW) halo the data allow has a virial mass of only  $3.9^{+3.1}_{-2.1} \times 10^{11} M_{\odot}$ , although the data are more consistent with models that have a slight radial anisotropy, which implies the galaxy has an even lower DM halo mass of  $2.2^{+2.0}_{-1.2} \times 10^{11} M_{\odot}$ . Modeling of the  $h_4$  Gauss-Hermite coefficient is inconclusive but seems to be consistent with mild radial anisotropy. A cored logarithmic DM halo with parameters  $r_0 = 7$  kpc and  $v_0 = 100$  km s<sup>-1</sup> can also reproduce the observed velocity dispersion profile. The MOND predictions overestimate the velocity dispersion. In conclusion, we cannot easily reproduce the previous findings of a predominance of DM in NGC 7507 within a simple spherical model. DM may be present, but only in conjunction with a strong radial anisotropy, for which there are some indications.

**Key words.** galaxies: individual: NGC 7507 – Galaxy: kinematics and dynamics

## 1. Introduction

The existence of dark matter (DM) in spiral galaxies (or alternatively a law of gravitation that differs from the Newtonian law) remains undisputed. However, the same cannot be said conclusively for *all* elliptical galaxies. Central galaxies in galaxy clusters such as NGC 6166 (Kelson et al. 2002), NGC 1399 (Richtler et al. 2008; Schuberth et al. 2010), and NGC 3311 (Richtler et al. 2011) are embedded in massive dark halos as is the case of bright non-central cluster ellipticals such as NGC 4636 and NGC 4374 in Fornax (Schuberth et al. 2006; Napolitano et al. 2010). In contrast elliptical galaxies with lower luminosities in sparser environments (NGC 821, 3379, 4494, 4697), whose mass profiles

have been studied using planetary nebulae (PNe) kinematics, appear to show only weak evidence of DM (Romanowsky et al. 2003; Douglas et al. 2007; Napolitano et al. 2009; Méndez et al. 2009; Teodorescu et al. 2010; but see Weijmans et al. 2009); although the case of NGC 3379 may be consistent with a normal cold DM halo if a very strong radial anisotropy is present (de Lorenzi et al. 2009).

The comparison of field, and possibly isolated, elliptical galaxies to those in clusters is of great interest. Different formation mechanisms may have led to differences in their dark halo structure, but observationally few properties have been reliably determined. Isolated galaxies may also be good test objects of the modified Newtonian dynamics (MOND, Milgrom 1983; Sanders & McGaugh 2002), since complications arising from the “external field effect” (Milgrom 1983; Wu et al. 2007) should be minimal.

The galaxy NGC 7507 is an elliptical (E0, de Souza et al. 2004) of  $M_V = -21.6$ , with a distance modulus of  $31.83 \pm 0.17$  based on surface brightness fluctuations ( $23.22 \pm 1.8$  Mpc; Tonry et al. 2001, corrected by  $-0.16$  mag following Jensen et al. 2003); we assume this distance throughout the paper, which implies a scale of  $112.5$  pc arcsec<sup>-1</sup>. The galaxy is fairly isolated, forming a probable pair with the SBb galaxy NGC 7513, which lies at a projected distance of 18 arcmin ( $\sim 130$  kpc), but displaying no signs of recent interactions (Tal et al. 2009). Due to its

\* Based on observations taken at the Gemini Observatory, which is operated by the Association of Universities for Research in Astronomy, Inc., under a cooperative agreement with the NSF on behalf of the Gemini partnership: the National Science Foundation (United States), the Science and Technology Facilities Council (United Kingdom), the National Research Council (Canada), CONICYT (Chile), the Australian Research Council (Australia), Ministério da Ciência e Tecnologia (Brazil) and SECYT (Argentina).

\*\* Tables 1–3 are available in electronic form at

<http://www.aanda.org>

\*\*\* Current address: Finnish Centre for Astronomy with ESO (FINCA), University of Turku, Väisäläntie 20, 21500 Piikkiö, Finland.

proximity and regular shape, its dynamics have been well studied leading to strikingly different conclusions. Bertin et al. (1994) found no evidence of a DM halo, using major-axis kinematical data out to  $66''$ . Kronawitter et al. (2000, hereafter K+00) performed dynamical analyses of 21 round elliptical galaxies, including NGC 7507. They concluded that models based on luminous matter could only be ruled out with 95% confidence for only three galaxies, including NGC 7507. Contradicting this finding, Magorrian & Ballantyne (2001) adopted the kinematics of Bertin et al. (1994) and photometry of Franx et al. (1989b) to establish that NGC 7507 has a constant mass-to-light ratio ( $M/L$ ) profile, i.e. that it does not contain a dark halo.

The most significant difference between these studies appears to be the observational data used and not the modeling approach, which, although different, should not give strongly discrepant results. We decided to obtain new, deeper long-slit spectroscopy using Gemini South. Eight-meter class telescopes have been scarcely used to measure the long-slit kinematics of the unresolved stellar components of elliptical galaxies (e.g. Thomas et al. 2007; Forestell & Gebhardt 2010; Pu et al. 2010; and see Samurović & Danziger 2005, for a review of the work made with 4 m class telescopes). Much effort has been put into kinematic studies of PNe (e.g. Méndez et al. 2009) and globular clusters (e.g. Romanowsky et al. 2009; Schuberth et al. 2010), which can be observed out to much larger galactocentric radii, but provide weaker constraints of their orbital anisotropies.

The paper is organized as follows: we present our observations and reduction procedures in Sect. 2. The photometric properties of the galaxy together with a description of its kinematics are given in Sect. 3. The dynamical modeling is presented in Sect. 4, while the discussion and conclusions can be seen in Sects. 5 and 6, respectively.

## 2. Observations and data reduction

### 2.1. CTIO/MOSAIC photometry and photometric calibration

The images used in this study were obtained with the MOSAIC II camera (an 8 CCDs mosaic imager, 16 amplifiers) mounted at the prime focus of the 4-m Blanco telescope at the Cerro Tololo Inter-American Observatory (CTIO, Chile). Observations were carried out during 2005 August 5–6, where the first night was “useful” and the second one “photometric”, according to the CTIO reports. One pixel of the MOSAIC wide-field camera subtends  $0.27$  arcsec on the sky, which corresponds to a field of  $36' \times 36'$ , i.e. approximately  $230 \times 230$  kpc<sup>2</sup> at the distance of NGC 7507.

All fields were imaged in Washington  $C$  ( $\lambda_{\text{central}} = 3850 \text{ \AA}$ ) and Kron-Cousins  $R$  ( $\lambda_{\text{central}} = 6440 \text{ \AA}$ ) filters. The  $R$  filter was used instead of the original Washington  $T_1$ , as Geisler (1996) has shown that the Kron-Cousins  $R$  filter is more efficient than  $T_1$ , and that  $R$  and  $T_1$  magnitudes are closely related, with just a very small colour term and zero-point difference ( $R - T_1 \sim -0.02$ ).

To fill in the gaps between the eight individual MOSAIC chips, the data were dithered taking four images in  $R$  with exposure times of 720 s each, and seven images in  $C$  with exposures of 1800 s each. To avoid saturation at the galaxy core, additional shorter exposures of 60 s in  $R$  and of 300 s in  $C$  were also obtained. Sky flats were obtained at the beginning and end of each night.

The MOSAIC data reduction was performed using tasks from the MSCRED package within IRAF. Several tasks were employed to correct for the variable pixel scale across the CCD, which might cause a 4 per cent variability in the point-sources

brightness (from the center to the corners). The final combined  $R$  image still shows sensitivity variations up to 1.4 per cent, and the final  $C$  image up to 3.0 per cent (peak-to-peak). The seeing in these final images is  $1.1''$  on the  $R$  frame, and  $1.3''$  on the  $C$  image.

The photometric calibration was performed with three fields of standard stars selected from the list of Geisler (1996), each containing 7 to 10 standard stars. For these fields,  $C$  and  $R$  images were obtained in each night, covering an airmass range 1.1–2.3. Finally, we used a single set of calibration equations for both nights.

The equations read

$$\begin{aligned} T_1 &= R_{\text{inst}} + (0.89 \pm 0.01) - (0.23 \pm 0.01)X_R \\ &\quad + (0.016 \pm 0.003)(C - T_1), \\ C &= C_{\text{inst}} + (1.55 \pm 0.01) - (0.30 \pm 0.01)X_C \\ &\quad + (0.069 \pm 0.003)(C - T_1), \end{aligned}$$

where  $C_{\text{inst}}$  and  $R_{\text{inst}}$  are instrumental magnitudes and  $X_C$  and  $X_R$  are the airmasses.

The absolute photometric quality of the  $C$ -photometry is dubious, hence it is only used for differential analyses. The  $R$ -photometry is of high quality, as the comparison of our results with previous photometric data sets of the galaxy reveals. The mean difference from Franx et al. (1989b) is 0.08 mag (Franx et al. is brighter). We also compare with photoelectric aperture measurements given by Poulain & Nieto (1994). In this case, we find that our profile is brighter by 0.15 mag.

### 2.2. Surface photometry

The surface photometry of the galaxy was performed using the IRAF/ELLIPSE task. The shallower images were used to determine the surface brightness profile for the inner  $\sim 10''$  in the  $C$  and  $R$  profiles, which were saturated in the longer exposures. The sky brightness in the shallow images was determined by taking the median value of the sky in several  $15 \times 15$  pixel boxes of empty regions further than  $5'$  from the galaxy center. Since an accurate sky determination is critical in shaping the light profile in the outer parts of a galaxy, a different procedure, similar to the one devised by Dirsch et al. (2003), was adopted for the deep images. First, DAOPHOT (Stetson 1987) was applied to all point sources present in the field. The local sky brightness of each source was determined using the median of the sky value of the pixels between 15 and 25 pixels from each source center. Deviant pixels were rejected using a three-sigma clipping procedure. All the sky values were then ordered according to their distance from the center of NGC 7507. To exclude overestimated sky values (of point sources close to nearby galaxies, bright stars or chip defects), a new iterative 3-sigma clipping was applied to the sky values within radial bins of 100 objects, this time using robust location and scale bi-weight estimators (Beers et al. 1990). At distances larger than  $5'$  from the center of the galaxy, the value of the sky brightness fluctuates by less than 0.5%. The final value for the sky was then taken as the mean of the sky values between  $10'$  and  $12'$  ( $\sim 78$ – $98$  kpc) from the galaxy center and the  $R$  sky brightness in mag/arcsec<sup>2</sup> was found to be 20.90. The photometry of the galaxy can be seen in Table 1.

### 2.3. Gemini/GMOS spectroscopy

Long-slit spectra of NGC 7507 were obtained using the Gemini Multi-Object Spectrograph (GMOS) on Gemini South, Cerro Pachón, Chile, in queue mode during the nights of September 19

and 21, 2004 (program GS-2004B-Q-75). The grism was the B600+\_G5323 which, in conjunction with a 1'' slit width, gives a resolution of  $\sim 4.7 \text{ \AA}$  FWHM. Three consecutive exposures of 1800s each were taken for a position angle of  $90^\circ$ , which is close to the major axis (PA =  $105^\circ$ ), and for PA =  $0^\circ$ , which is close to the minor axis (PA =  $15^\circ$ ). For convenience, these two positions are referred to hereafter as the major and minor axes, respectively. Standard reduction steps (bias subtraction, flat fielding, detectors mosaicing, wavelength calibration) were performed with the Gemini IRAF package (v 1.9.1). Typical wavelength residuals were  $\sim 0.05 \text{ \AA}$ . No cosmic ray cleaning was attempted at this stage because it introduced undesired noise, especially around bright sky lines. Since copper-argon arc spectra were taken during daytime and not immediately either after or before the science exposures, a correction of the zero point of the wavelength solution was necessary and was performed by measuring the position of the bright sky line at  $5577.34 \text{ \AA}$ . This correction typically amounted to  $0.1 \text{ \AA}$ . After that, the three spectra for each position angle were averaged. Sky subtraction was done using the IRAF task background, by averaging 50 rows on opposite sides of each spectra, at around  $4.5'$  from the galaxy center for the major axis and  $\sim 4'$  for the minor axis. The two-dimensional (2D) spectra were spatially rebinned to achieve a constant  $S/N \sim 50/\text{pixel}$ , which is highly desirable when measuring the higher order moments of the line-of-sight velocity distribution (LOSVD). The  $4800\text{--}5500 \text{ \AA}$  wavelength range, which contains strong absorption features as H $\beta$ , Mg  $b$ , and Fe lines around  $5325 \text{ \AA}$ , was selected for the kinematical analysis.

Mean velocity, velocity dispersion and higher order moment profiles were measured for both long slits by using the Gauss-Hermite pixel fitting code (van der Marel 1994, hereafter vdM code) and the penalized pixel fitting (pPXF) method developed by Cappellari & Emsellem (2004). Both approaches have the advantage of performing their calculations in pixel space instead of Fourier space, thus allowing a more precise masking of undesired zones in the spectra (emission lines, bad columns, etc.). Both methods also parametrize the LOSVD in terms of a Gauss-Hermite series (Gerhard 1993; van der Marel & Franx 1993). The former algorithm measures the mean velocity and the velocity dispersion, and, with these values fixed, fits the higher order terms of the velocity distribution, parametrized by the Gauss-Hermite coefficients  $h_3$  and  $h_4$ . The latter algorithm fits all parameters simultaneously, but can bias the solution to a Gaussian shape when the higher order terms are not sufficiently constrained by the data (Cappellari & Emsellem 2004). An advantage of the pPXF method over the vdM code is that it can perform the fitting process with a linear combination of template spectra, minimizing the effect of template mismatching.

A subset of 22 old and metal-rich single stellar population models from Vazdekis et al. (2010) based on the MILES stellar library (Sánchez-Blázquez et al. 2006) were used as velocity templates for our analysis using the vdM code. These templates were logarithmically rebinned to the same dispersion and convolved with a Gaussian to ensure that they had the same spectral resolution as the science spectra. Final values of mean velocity, velocity dispersion,  $h_3$  and  $h_4$  parameters were assumed to be the average of the values for the three templates that provided the closest fit (the lowest  $\chi^2$  values).

In the pPXF analysis, two different sets of spectra were employed as templates to extract the kinematical information, the aforementioned Vazdekis et al. models, but this time the entire library consisting of 350 models, and the full MILES spectral library (Sánchez-Blázquez et al. 2006). Both have a spectral

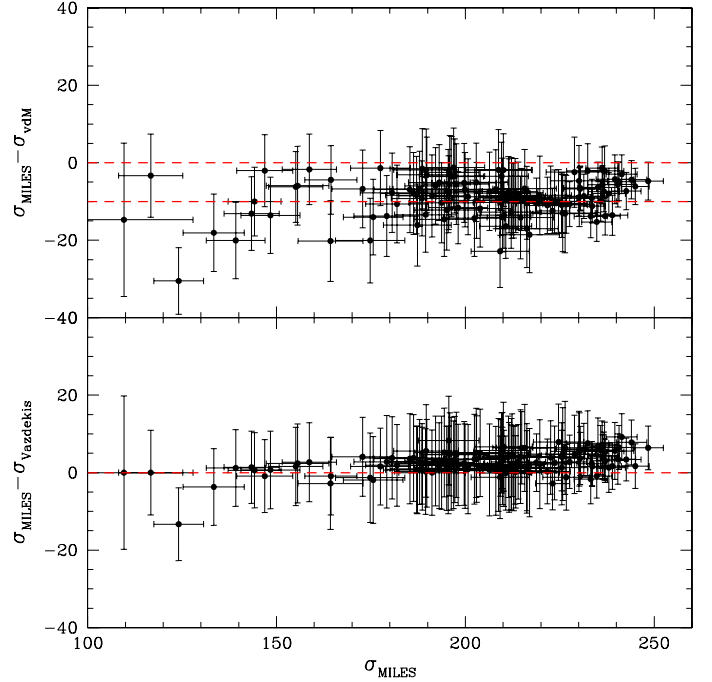


**Fig. 1.** Comparison between the different measurements of the velocity dispersion profile of the major axis of NGC 7507 as described in the text.

resolution of  $2.3 \text{ \AA}$  FWHM (but see Beifiori et al. 2011). Since we expect to find a population gradient across the galaxy (see Sect. 3), the templates used for each radial bin were not fixed, but freely chosen by pPXF from the MILES library and the Vazdekis models, separately, until the closest model was achieved. For the Vazdekis models, pPXF used typically 3 from the 350 models, while a mean number of 16 template stars from the 985 in the MILES library were used by pPXF for each radial bin. Estimations of the errors for all the calculated values were obtained by performing 100 Monte Carlo simulations in which random noise was added to each science spectrum and then passed again through pPXF (e.g. Cappellari & Emsellem 2004; Bedregal et al. 2006). In this case, only the templates that were previously selected by pPXF were fitted, and not the entire set. The dispersion in the values obtained from the simulations are quoted as the error bars in the measurements from the original spectra.

The agreement between the results of pPXF using the two sets of templates is very good. However a few remarks are appropriate. Typically pPXF uses much fewer templates from the Vazdekis models ( $\sim 3$ ) and the  $\chi^2$  values are always larger than when using MILES. The inclusion of multiplicative Legendre polynomials reduces the  $\chi^2$ , but does not increase the number of templates used. We find a systematic small difference of  $3 \text{ km s}^{-1}$  between the velocity dispersion results obtained using the Vazdekis SSP models and the MILES library (Fig. 1, bottom panel). The difference from the values given by the vdM code is somewhat larger: the velocity dispersions derived with vdM are systematically larger. We find a systematic difference of  $9 \text{ km s}^{-1}$  (Fig. 1, top panel). Since template mismatching is expected to be far less significant for this method, if not totally negligible, based on previous studies (e.g. Shapiro et al. 2006; Cappellari et al. 2007), we decided to adopt the results obtained using the MILES spectral in all the subsequent kinematic description and dynamical analyses. These measurements can be seen in Tables 2 and 3.

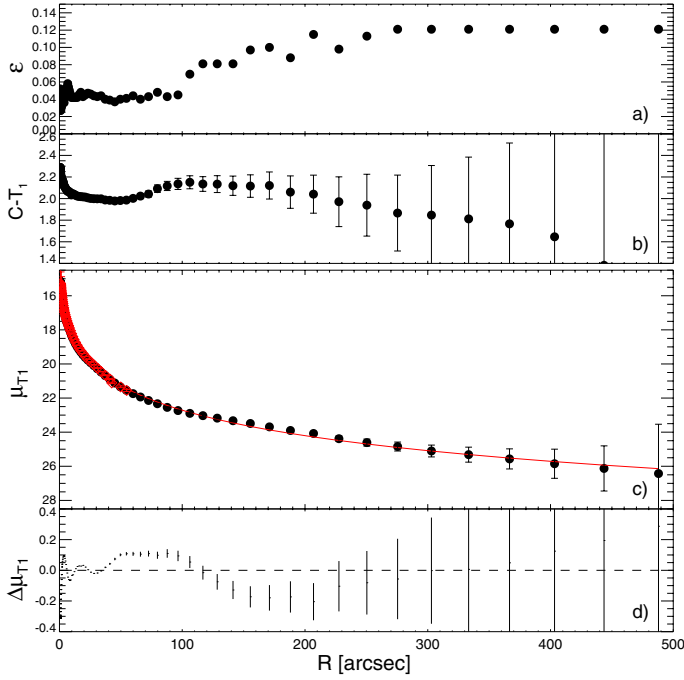


**Fig. 2.** CTIO/MOSAIC surface photometry of NGC 7507. **a)** Ellipticity profile. **b)**  $C - R$  color profile. **c)**  $R$  surface brightness profile (black circles) and  $R$  surface photometry from Franx et al. (1989b) (filled red squares). The solid red line is the fit of a double  $\beta$  model to our data. Residuals can be seen in panel **d)**.

### 3. Results

#### 3.1. Light and color profile

There is a well-established variety of analytical model light profiles of elliptical galaxies. Since we wish to use the light profile within a spherical Jeans analysis, its analytical form, besides being an excellent representation, should permit a closed analytical deprojection as well as an analytical mass profile. These conditions are fulfilled by the sum of two  $\beta$  profiles (or Hubble-Reynolds profile)

$$\mu(R) = -2.5 \log \left\{ a_1 \left( 1 + \left( \frac{R}{R_1} \right)^2 \right)^{-1} + a_2 \left( 1 + \left( \frac{R}{R_2} \right)^2 \right)^{-1} \right\}, \quad (1)$$

where  $a_1 = 2.052 \times 10^{-8}$ ,  $a_2 = 6.452 \times 10^{-7}$ ,  $R_1 = 16''$ , and  $R_2 = 2.19''$ , provide an excellent representation of the surface brightness profile between  $2''$  and  $400''$  (Fig. 2, panel c).

Although the  $\beta$ -profile provides an excellent description out to about 50 kpc, the extrapolation to larger radii, which is used in the dynamic modeling, is not a priori justified. It is generally unknown where a galaxy “ends” (but see the remarks in Sect. 4.1). The mass of the  $\beta$ -model diverges for large radii. This raises the concern of whether systematic errors are introduced by extrapolating the profile to larger radii.

We therefore fit the surface brightness profile with the sum of two Sersic profiles

$$I(R) = I_0 \exp \left( - (R/a_s)^{1/m} \right) \quad (2)$$

(Sersic 1968; Graham & Driver 2005), since a single Sersic profile fails to accurately reproduce the luminosity in the entire radial range, underestimating the outer ( $\gtrsim 20$  kpc) profile. The Sersic parameters are  $I_0^i = 1.90 \times 10^6 L_\odot \text{ pc}^{-2}$ ,  $a_s^i = 0.0677 \text{ pc}$ ,

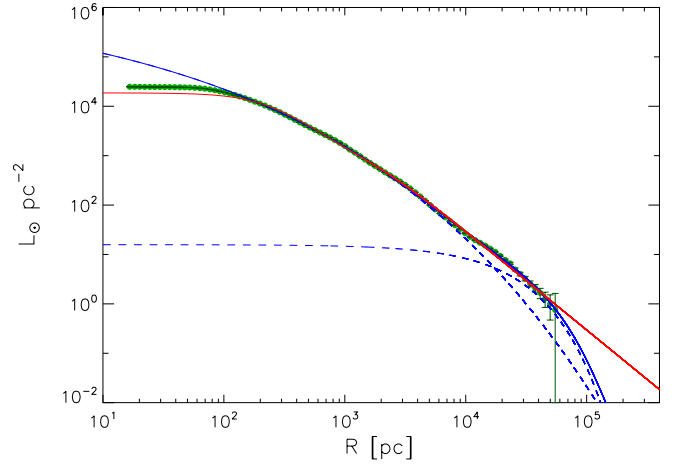


**Fig. 3.** Surface brightness profile of NGC 7507. The green dots indicate the  $R$  photometry in units of  $L_\odot \text{ pc}^{-2}$ . The dashed blue lines represent the two Sersic profiles, while the solid blue line is their sum. The red solid line represents the double  $\beta$  model.

$m^i = 4.8$ , for the inner Sersic profile, and  $I_0^o = 15.77 L_\odot \text{ pc}^{-2}$ ,  $a_s^o = 15832 \text{ pc}$ ,  $m^o = 1.05$ , for the outer profile;  $M_{\odot,R} = 4.42$  (Binney & Merrifield 1998) was adopted.

Both models provide excellent descriptions of the surface density profile from  $\sim 200 \text{ pc}$  ( $\sim 1.5''$ ) until the last photometric point at  $\sim 55 \text{ kpc}$ , and are practically indistinguishable (see Fig. 3). Differences are seen only in the inner  $\sim 200 \text{ pc}$  where the double  $\beta$  model underestimates the light profile, while the opposite happens with the double Sersic model and for the extrapolation of the light profile (outside  $\sim 55 \text{ kpc}$ ) where the double  $\beta$  model falls as  $R^{-2.0}$ , but the Sersic profile declines more steeply.

The double Sersic profile implies that the effective radius is  $R_e = 75''$ . This is significantly larger than the previous estimations of  $24''$  (Lauberts & Valentijn 1989),  $31''$  (Faber et al. 1989), and  $47''$  (de Souza et al. 2004); this is unsurprising given our deep imaging. For example, the value of Faber et al. is taken from the RC2 (de Vaucouleurs et al. 1976) where the total galaxy brightness is defined as the brightness within an isophote with a surface brightness in the  $B$ -band of  $25 \text{ mag arcsec}^{-2}$  which we found for NGC 7507 occurs at a distance of about  $150''$ .

The color profile was evaluated as the difference between the two models in  $C$  and  $R$  (Fig. 2, panel b). The inner core (within  $10''$ ) declines by  $0.3 \text{ mag}$  with radius to bluer colors, followed by a radial interval of more or less constant color. The color then gets redder again at about  $50''$ , and remains practically unchanged out to  $200''$ . The outer gradient to bluer colors might exist, but owing to the large uncertainties cannot be claimed convincingly. Color profiles for the inner  $50''$  were given by Franx et al. (1989b) and Goudfrooij et al. (1994). The inner strong gradient is apparent in both of them, but the gradient of almost  $0.5 \text{ mag}$  in  $B - I$  between  $30''$  and  $60''$  seen by Goudfrooij et al. (1994) is not found in our color profile.

It is interesting to consider a 2D color image of the inner region. Figure 4 was obtained by dividing the short  $C$  by the  $R$  exposures. It is apparent that the “color field” is not spherically symmetric but tends to have bluer colors along the E-W axis. One could therefore interpret the plateau with  $C - R = 2.0$  between  $10''$  and  $50''$  as a result of averaging along isophotes, before the color gets redder again. We are unable to determine, however, whether diffuse dust or population effects or both are responsible.

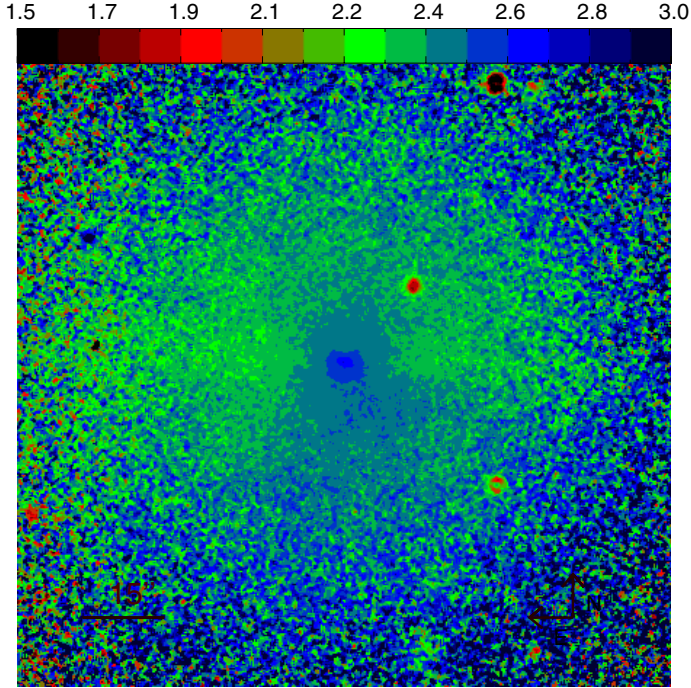


**Fig. 4.**  $C - R$  color image of NGC 7507 based on the short exposures. Image has been median smoothed in  $3 \times 3$  pixel boxes. Image size is  $2' \times 2'$ .

### 3.2. Ellipticity and higher isophote moments

As all previous studies have pointed out, the galaxy in projection is very round. We find  $\langle \epsilon \rangle = 0.045 \pm 0.008$ , where the mean is taken over the inner  $2'$ , avoiding the innermost  $2''$  which are affected by seeing. Beyond  $2'$  the ellipticity slightly increases, partly due to the difficulty in masking a bright 11th mag star, located  $\sim 6'$  SE of the galaxy (Fig. 2, panel a).

The Fourier coefficient  $a_4$  describes the isophote's boxiness or diskyness (negative: boxy; positive: disk). It is zero out to  $2'$ . The slight boxiness at larger radii may also be caused by the bright star. A table with the photometry, including ellipticities, PA, and  $a_4$  is available in Table 1.

### 3.3. Irregular features

A small, slightly off-centered dip in the light can be seen in the shallow  $R$  image. It is not apparent in the shallow  $C$  image, which has poorer seeing. We interpret this as a dust lane already detected by Franx et al. (1989b).

Tal et al. (2009) found evidence of a faint shell north of the galaxy. However, when the smoothed 2D model created with IRAF\BMODEL task is subtracted from the galaxy light, we see this shell in neither the  $C$  nor in the  $R$  images. No substructure was detected either in the shallower images analyzed by de Souza et al. (2004).

### 3.4. Stellar kinematics

The kinematics along the major axis of NGC 7507 have been measured by several groups (Bertin et al. 1994; Franx et al. 1989a, K+00); but along the minor axis only by Franx et al. (1989a) and higher order moments only by K+00. We extended the radial coverage of Franx et al. (1989a) by a factor of 1.5 for the major axis and 2.5 for the minor axis.

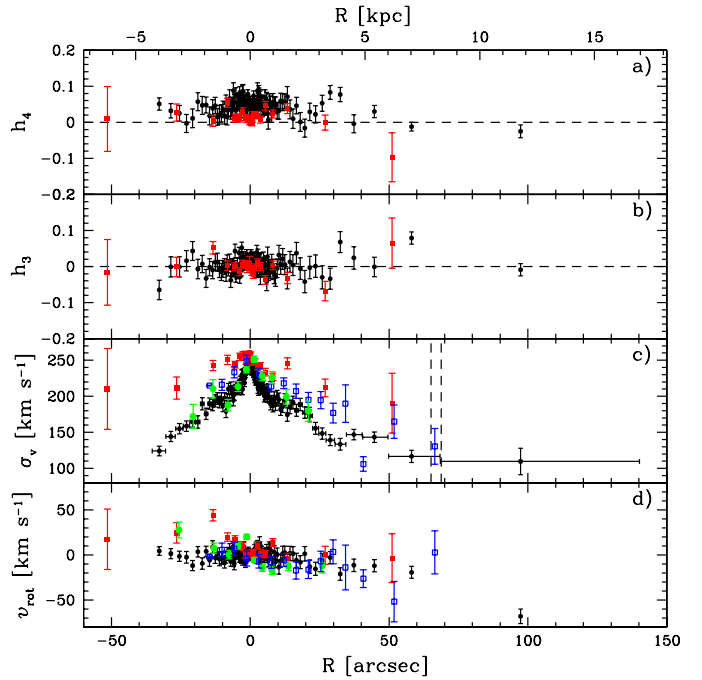


**Fig. 5.** Major axis kinematics of NGC 7507, as extracted with pPXF (see text). **a)** Hermite coefficient  $h_4$  profile, **b)**  $h_3$  profile, both panels show a dashed line at the zero level for comparison, **c)** velocity dispersion. The horizontal error bars show the regions across which the spatial binning was done (shown only in this panel, but valid for all four). The vertical dashed strip indicates a gap between the detectors in which no measurements are possible, **d)** rotation profile. For all panels, open black circles are our data, red solid squares are from K+00, solid green circles are from Franx et al. (1989a), and blue open squares come from Bertin et al. (1994).

#### 3.4.1. Rotation

The major axis rotation is very low (Fig. 5, panel d), consistent with no rotation, with a formal amplitude of  $-1 \pm 6 \text{ km s}^{-1}$  within the inner  $30''$ . In the  $30\text{--}60''$  range, the amplitude slightly increases to a value of  $-13 \pm 7 \text{ km s}^{-1}$ , which is consistent with the aforementioned previous studies. The outermost measured bin, at a mean distance of  $97''$  shows a significant increase in the rotation with respect to the center ( $-68 \pm 8 \text{ km s}^{-1}$ ). This may be partly due to the misalignment of the slit direction and the photometric major axis but perhaps also a hint that the kinematic properties of the galaxy suffer a change at large radii, as seen for example in NGC 821 and NGC 1400 (Proctor et al. 2009).

The minor axis rotation is pronounced and slightly asymmetric with amplitudes of  $30 \pm 7 \text{ km s}^{-1}$  in the west direction and  $-43 \pm 7 \text{ km s}^{-1}$  in the east direction inside the range  $5\text{--}50''$  (Fig. 6, panel d). Franx et al. (1989a) measured an amplitude of  $36 \pm 5 \text{ km s}^{-1}$  in the range  $5\text{--}30''$ , without detecting any asymmetry. In the outermost east and west bins, around  $60''$ , the mean velocity is consistent with no rotation. This rotation profile closely resembles the major axis rotation of NGC 3379 (Statler & Smecker-Hane 1999; Weijmans et al. 2009, their Fig. 4).

Summarising, the isophote shapes are sufficiently undisturbed and the projected rotation amplitude is small enough to justify the use of a non-rotating, spherical mass model.

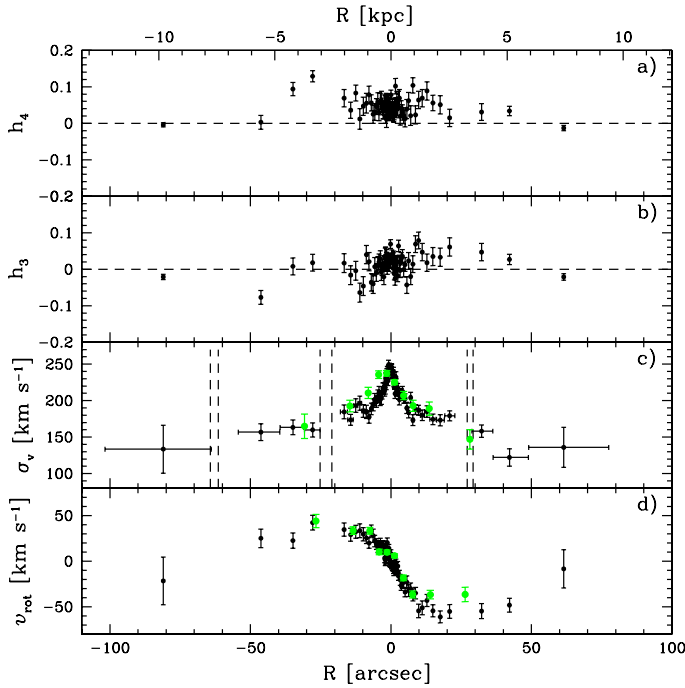


**Fig. 6.** Minor axis kinematics of NGC 7507. The vertical dashed strips show the positions of the gaps between detectors and two interloping background galaxies, which were masked in the spatial binning process. Symbols are the same as in Fig. 5.

### 3.4.2. Velocity dispersion

The major axis velocity dispersion rapidly declines in the inner 30'' and undergoes a slower decline at larger radii. The dispersion values of K+00 deviate strongly, not only from our values, but also from Franx et al. (1989a) and Bertin et al. (1994) (Fig. 5, panel c). While the difference at the center of the galaxy is roughly within errors ( $9.7 \pm 4.8 \text{ km s}^{-1}$ ), and it can be easily explained by the spectra being taken under different seeing conditions; at 27'' from the center, the difference amounts to  $70 \pm 14 \text{ km s}^{-1}$  in the sense that K+00 values are larger than ours.

The minor axis velocity dispersion profile shows a similar rapid decline in the inner 30'' but a less steep decline at larger radii (Fig. 6, panel c). As in the case of the major axis, the difference from Bertin et al. (1994) is minimal and amounts to  $14 \pm 24 \text{ km s}^{-1}$ , where the uncertainty is caused almost entirely by the Bertin et al. (1994) values.

A kinematic classification of early-type galaxies, based on an angular momentum proxy was introduced by Emsellem et al. (2007). They defined

$$\lambda_R = \frac{\sum F_i R_i |V_i|}{\sum F_i R_i \sqrt{V_i^2 + \sigma_i^2}}, \quad (3)$$

where  $F_i$  is flux,  $R_i$  is distance to the center of the galaxy, and  $V_i$  and  $\sigma_i$  are the mean velocity and velocity dispersion. Emsellem et al. (2007) found that early-type galaxies can be separated into two classes of slow and fast rotators, depending on whether they have  $\lambda_R$  values below (slow) or above (fast) 0.1 inside  $R_e$ . Even though this parameter was introduced for the SAURON 2D data, it can be applied to long-slit measurements in order to help us to compare with the original definition, once a proper scaling factor of 0.57 is applied (Cappellari et al. 2007; Coccato et al. 2009). In that case the sum is over the quantities along the slit.

We calculated the  $\lambda_R$  parameter separately for each long slit position. For both axes, the parameter mildly increases inside  $R_e$  reaching  $\lambda_{R_e}^{\min} = 0.088$  and  $\lambda_{R_e}^{\max} = 0.018$ , staying basically flat beyond that radius. This is consistent with the mild rotation of the galaxy. NGC 7507 can be classified as a slow rotator, sharing also the kinematic misalignment which is often seen in these galaxies, although it has a rapidly declining velocity dispersion profile which is more common amongst fast rotators (Coccato et al. 2009).

### 3.4.3. Higher order moments

The Gauss-Hermite coefficient  $h_3$ , which measures the asymmetric deviation from a Gaussian, is consistent with being zero along the major axis. Along the minor axis within 20'', it appears to have a gradient which would be consistent with its rotation (Fig. 6, panels b and d).

The coefficient  $h_4$ , which indicates symmetric deviations from a Gaussian profile, is positive for both the major and minor axis spectra. The sign agrees with the measurements of K+00, who also found slightly positive values of  $h_4$ , although their values were somewhat smaller (Fig. 5, panel a). We return to this result when discussing any possible anisotropies.

## 4. Dynamical modeling

### 4.1. The stellar mass profile

To obtain the (spherical) stellar mass profile we have to deproject the surface brightness profile after correcting for Galactic absorption ( $A_R = 0.128$ ; Schlegel et al. 1998). In the case of the double- $\beta$  profile this is achieved by applying the Abel deprojection formula, which for the  $\beta$  profile has an analytical description

$$j(r) = \frac{C_R}{2} \sum_{i=1}^2 \frac{a_i/R_i}{[1 + (r/R_i)^2]^{3/2}}, \quad (4)$$

where  $a_i$  and  $R_i$  come from Eq. (1), and  $C_R = 2.5 \times 10^{10}$  is the factor used to transform to units of  $L_\odot \text{ pc}^{-2}$ , adopting  $M_{\odot, R} = 4.42$  (Binney & Merrifield 1998). The enclosed stellar mass can be obtained by integrating this light density

$$M_\star(r) = 4\pi \int_0^r \Upsilon_{\star, R}(r) j(r) r^2 dr, \quad (5)$$

where  $\Upsilon_{\star, R}$  is the stellar  $M/L_R$ . For constant  $M/L_R$ , this integral has the exact solution

$$M_\star(r) = 2\pi C_R \Upsilon_{\star, R} \sum_{i=1}^2 a_i R_i^2 \left( \sinh^{-1} x_i - \frac{x_i}{\sqrt{x_i^2 + 1}} \right), \quad (6)$$

where  $x_i = r/R_i$  and  $a_i$  and  $R_i$  have the same meaning as in Eq. (4).

The stellar  $M/L_R$  appears as a parameter in the fit to the kinematical data, adopting the deprojected light profile and certain forms for a possible DM halo. From the shape of the colour profile, one concludes that  $M/L$  as a population property is approximately constant out to a radius of 2'. At larger radii, the  $M/L$  may drop owing to a declining metallicity. However, this is only weakly constrained and any effect on the inner projected velocity dispersion would be completely degenerate with a dark halo.

The Sersic profile can be deprojected using an approximation given by [Prugniel & Simien \(1997\)](#)

$$\begin{aligned} j(r) &= j_1 \tilde{j}(r/a_s), \\ \tilde{j}(x) &\simeq x^{-p} \exp(-x^{1/m}), \\ j_1 &= \left\{ \frac{\Gamma(2m)}{\Gamma[(3-p)m]} \right\} \frac{I_0}{2a_s}, \\ p &\simeq 1 - 0.6097/m + 0.05463/m^2, \end{aligned}$$

where the latter equation comes from [Lima Neto et al. \(1999\)](#),  $\Gamma(x)$  is the Gamma function, and  $I_0$ ,  $a_s$ , and  $m$  refer to the Sersic parameters from Eq. (2). We also refer to [Mamon & Łokas \(2005b\)](#) for a compilation of the relevant formulae.

Integrating the luminosity density,  $j(r)$ , the enclosed luminosity is found. [Lima Neto et al. \(1999\)](#) give

$$L_s(r) = L_{\text{tot}} \tilde{L}_s(r/a_s), \quad (7)$$

$$\tilde{L}_s(x) = \frac{\gamma[(3-p)m, x^{1/m}]}{\Gamma[(3-p)m]}, \quad (8)$$

where  $\gamma$  is now the incomplete Gamma function and

$$L_{\text{tot}} = 2\pi m \Gamma(2m) I_0 a_s^2 \quad (9)$$

is the total luminosity of the profile. For our double Sersic profile, the luminosity is simply the sum of the luminosity of both the inner and outer Sersic profiles.

Since beyond  $\sim 55$  kpc the double- $\beta$  and Sersic profiles display the most distinct behaviors (cf. Fig. 3), we inspected the influence of these dissimilar extrapolations on their respective enclosed luminosities, which are directly related to the stellar mass through the  $M/L$ . Figure 7 considers the enclosed luminosities of both models normalized to the total luminosity of the double Sersic model given by Eq. (9). As expected from Fig. 3, the luminosities are very similar not only within the  $\sim 55$  kpc where the galaxy light was directly measured, but well beyond. A  $\sim 10\%$  difference in the total enclosed luminosity is reached only at 200 kpc. In practice, however, the extension of elliptical galaxies may be lower than this limit. In NGC 4636, for example, the globular cluster distribution is cut-off at about  $\sim 60$  kpc ([Dirsch et al. 2005](#)). A similar behavior has been seen in M 87, the central galaxy of Virgo, where the planetary nebulae distribution show a truncation of the stellar halo at  $\sim 150$  kpc ([Doherty et al. 2009](#)). Therefore, any differences in the extrapolations beyond 200 kpc are not relevant to a dynamical analysis of the galaxy.

Given the similarities between the light profiles and to avoid any uncertainties introduced by the approximations used in the Sersic profile deprojection (which are not present in the analytic form of the  $\beta$  profile deprojection), the Jeans analysis that we now describe was based on the stellar distribution given by the  $\beta$  model profile. In any case, the velocity dispersions shown in Fig. 8 were found to vary by less than  $2 \text{ km s}^{-1}$  at the most distant kinematic point, when the double Sersic model was used a basis of the stellar mass profile.

#### 4.2. Jeans analysis

The basis of our modeling is the spherical Jeans equation, which is strictly valid only for infinite, non-rotating systems. Its solutions, when applied to real galaxies, may be considered as good approximations, but there is no guarantee that they correspond to physically correct distribution functions. Moreover, the potential and the orbital anisotropy are degenerate, although we

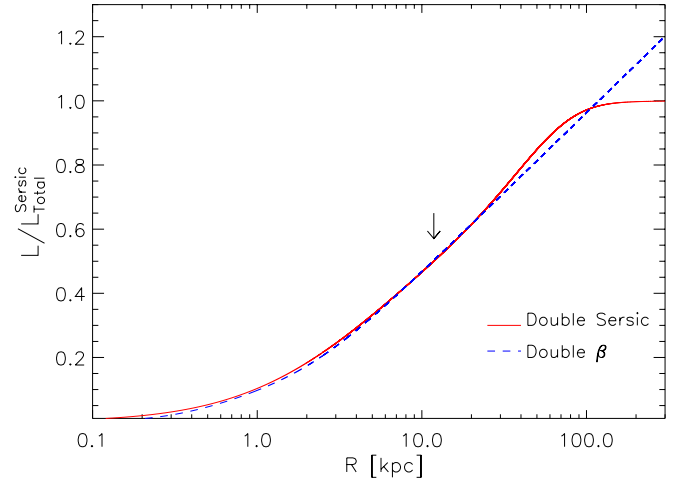


**Fig. 7.** A comparison between the enclosed luminosities of the double  $\beta$  profile (dashed blue line) and the double Sersic profile (red solid line), normalized to the double Sersic total luminosity. The arrow indicates the last spectroscopic point measured on the major axis.

refer to [Hansen & Moore \(2006\)](#) and the remarks below. On the positive side, this equation has an appealing simplicity, known anisotropies of elliptical galaxies in the inner regions are generally small (e.g. [Gerhard et al. 2001](#); [Cappellari et al. 2006](#)) and one can use the higher moments of the velocity distribution as constraints of the anisotropy. [Cappellari et al. \(2006\)](#) also demonstrated that more sophisticated dynamical modeling does not reveal grossly different results. The main uncertainty probably does not arise from the modeling approach, but collectively from the distance uncertainty, the quality of the data, and the assumption of sphericity.

For convenience and clarity, we give in the following the basic formulae. The Jeans equation is (e.g. [Binney & Tremaine 2008](#))

$$\frac{d[j(r)\sigma_r^2(r)]}{dr} + \frac{2\beta(r)}{r} j(r)\sigma_r^2(r) = -j(r)\frac{GM(r)}{r^2}, \quad (10)$$

which relates the light distribution,  $j(r)$ , and radial velocity dispersion,  $\sigma_r(r)$ , with the underlying gravitational potential or enclosed total mass,  $M(r)$ , and where

$$\beta(r) = 1 - \sigma_\theta^2/\sigma_r^2 \quad (11)$$

is the anisotropy parameter, which indicates possible departures from pure isotropy in the form of radial ( $\beta > 0$ ) or tangential ( $\beta < 0$ ) orbits.

For a given light and mass distribution, and a constant anisotropy, the solution to the Jeans equation is

$$j(r)\sigma_r^2(r) = G \int_r^\infty \frac{j(s)M(s)}{s^2} \left(\frac{s}{r}\right)^{2\beta} ds \quad (12)$$

(e.g. [Mamon & Łokas 2005b](#), hereafter MŁ05), which is then projected to be compared with the velocity dispersion measurements

$$\sigma_{\text{LOS}}^2(R) = \frac{2}{I(R)} \left[ \int_R^\infty \frac{j\sigma_r^2 r dr}{\sqrt{r^2 - R^2}} - R^2 \int_R^\infty \frac{\beta j\sigma_r^2 dr}{r \sqrt{r^2 - R^2}} \right] \quad (13)$$

([Binney & Mamon 1982](#)). For the anisotropy profiles adopted in Sects. 4.4 and 4.5, Eqs. (12) and (13) can be combined to yield the single integral solution

$$\sigma_{\text{LOS}}^2(R) = \frac{2}{I(R)} \int_R^\infty K(R, r) j(r) M(r) \frac{dr}{r}, \quad (14)$$

where the kernels  $K$  for the different anisotropy models are provided in Appendix A2 of (Mamon & Lokas 2005b).

The accuracy of the models can be quantified by the use of a simple  $\chi^2$  test

$$\chi^2 = \sum_i^{N_{\text{data}}} \left( \frac{\sigma_i^{\text{obs}} - \sigma_i^{\text{model}}}{\delta\sigma_i^{\text{obs}}} \right)^2, \quad (15)$$

where  $\sigma^{\text{obs}}$  is the measured velocity dispersion,  $\sigma^{\text{model}}$  is the predicted dispersion at the same radial distance,  $\delta\sigma^{\text{obs}}$  is the observational error associated with the dispersion measurement, and the sum is taken over all radial bins.

Under the spherical Jeans analysis, additional constraints on the dynamical behavior of the galaxy can be obtained by modeling the higher order moment of the velocity distribution which can be related to the Gauss-Hermite coefficient  $h_4$  (van der Marel & Franx 1993). For this, the higher order Jeans equations must be solved. This task can be achieved only if additional information about the distribution function is known. In particular, by assuming distribution functions of the form  $f(E, L) = f_o(E)L^{-2\beta}$  with constant  $\beta$ , it is possible to reduce the two higher-order Jeans equation to only one. A more detailed discussion, as well as the relevant formulae can be seen in Lokas (2002) and Napolitano et al. (2009). Our results using this approach are presented and discussed in Sect. 4.6.

#### 4.3. The velocity dispersion profile

To construct the radial dependence of the velocity dispersion profile, we averaged for a given radial bin the dispersion along the major and the minor axis (although the ellipticity is tiny) from Figs. 5 and 6. The dispersion values are symmetrical with respect to the galaxy center and are in agreement between the both axes when errors are considered. The bins are chosen in such a way that the inner region, where the S/N is highest, has the densest binning while the outer radii are covered with larger bins. The principal uncertainties are those in the mean values calculated by pPXF. Final values are listed in Table 4, which also lists the adopted  $h_4$  values. Their uncertainties are the standard deviations of the  $h_4$  values in the respective bins.

#### 4.4. Models without DM

The simplest model is the one in which  $M(r) = M_\star(r)$  (i.e. no DM) and  $\beta = 0$  (orbital isotropy). One can adopt the expected value for the  $M/L$  from an stellar populations analysis (which is a hypothetical value) or treat it as a free parameter in the Jeans equation solution, which is the procedure we chose here. This gives an upper limit to the stellar  $M/L$ . This model is shown as the black solid line in Fig. 8 (top left panel). It uses an  $M/L_R = 3.13$  and already gives a very good description of the dispersion profile with  $\chi^2 = 46.8$  for 16 degrees of freedom, where the statistics is calculated outside 400 pc, which is the radius where the data are no longer affected by seeing.

When the anisotropy was allowed to vary, we obtained almost the same  $M/L_R$  of 3.11 and  $\beta = 0.12$ , which is a slightly better fit (red dotted line). Table 5 shows the parameters for different best-fit models. An unrealistic totally radial model ( $\beta = 1$ ) is also shown in Fig. 8 as a comparison (blue dashed line).

From theoretical considerations (e.g. Abadi et al. 2006), elliptical galaxies are expected to have an anisotropy profile that is increasingly radially biased with growing radius. An analytical

**Table 4.** Adopted velocity dispersion,  $\sigma$ , and  $h_4$  values and their respective uncertainties.

Radius (arcsec)	$\sigma$ (km s <sup>-1</sup> )	$\Delta\sigma$ (km s <sup>-1</sup> )	$h_4$	$\Delta h_4$
0.5	239	2	0.051	0.013
1.5	232	2	0.045	0.013
2.5	222	2	0.010	0.017
3.5	217	2	0.005	0.018
4.5	211	2	0.002	0.011
5.5	205	2	0.055	0.014
6.5	202	2	0.043	0.027
7.5	199	2	0.042	0.016
8.5	189	2	0.043	0.019
9.5	193	2	0.033	0.012
10	191	2	0.040	0.015
13	190	2	0.048	0.026
16	181	2	0.037	0.026
22	167	2	0.019	0.023
28	153	2	0.042	0.036
42	141	3.3	0.044	0.033
52	135	6.7	0.008	0.022
62	131	14.3	-0.012	0.036
85	125	18.7	-0.013	0.015

**Notes.** We refrain from giving the  $h_3$ -values since they are not modeled.

profile with this characteristic was introduced by MŁ05 as

$$\beta_{\text{ML}}(r) = \beta_0 \frac{r}{r + r_a}, \quad (16)$$

with  $\beta_0 \sim 0.5$  and  $r_a \sim 1.4R_e$  when fitted to the merger simulations of Dekel et al. (2005). Another profile frequently used is the Osipkov-Merritt anisotropy model (Osipkov 1979; Merritt 1985),

$$\beta_{\text{OM}}(r) = \frac{r^2}{r^2 + r_a^2}, \quad (17)$$

where  $r_a$  is a characteristic radius marking the transition to outer radially biased orbits in both cases. Since the data do not really constrain the value for  $r_a$ , we fixed it to  $r_a = 1.4R_e$ , using  $R_e = 31''$ , from Faber et al. (1989). Even though our derived effective radius is significantly larger (see Sect. 3.1), we use this older estimation since it has been used in the previous studies of the galaxy, and also because it implies a faster transition to a radial behavior. The predictions from the Jeans equation using these anisotropies are shown in Fig. 8 (top left panel). The MŁ05 anisotropy gives a good description for the dispersion profile (green dashed line), but formally not better than the constant  $\beta = 0.12$  model. It reaches a value of  $\beta = 0.33$  at the outermost kinematic point. However, the Osipkov-Merritt anisotropy (green dash-dotted line) overpredicts the dispersion for the inner regions and underpredicts it for larger radii, making it less preferable as a realistic description within the context of this model.

An interesting relation between anisotropy  $\beta$  and the logarithmic density slope  $\alpha$  of a spheroidal system near equilibrium has emerged from DM simulations. Hansen & Moore (2006) found  $\beta(\alpha) = 1 - 1.15(1 + \alpha/6)$ , albeit with some scatter. This relation has also been analyzed by Mamon et al. (2006) for ellipticals formed in simulations of mergers of spirals consisting of stars, gas and DM. They found different results for the DM, but a quite similar relation for the stellar density distribution. If this were universal, the dynamical analysis of spherical systems would be greatly facilitated. We apply the above relation to

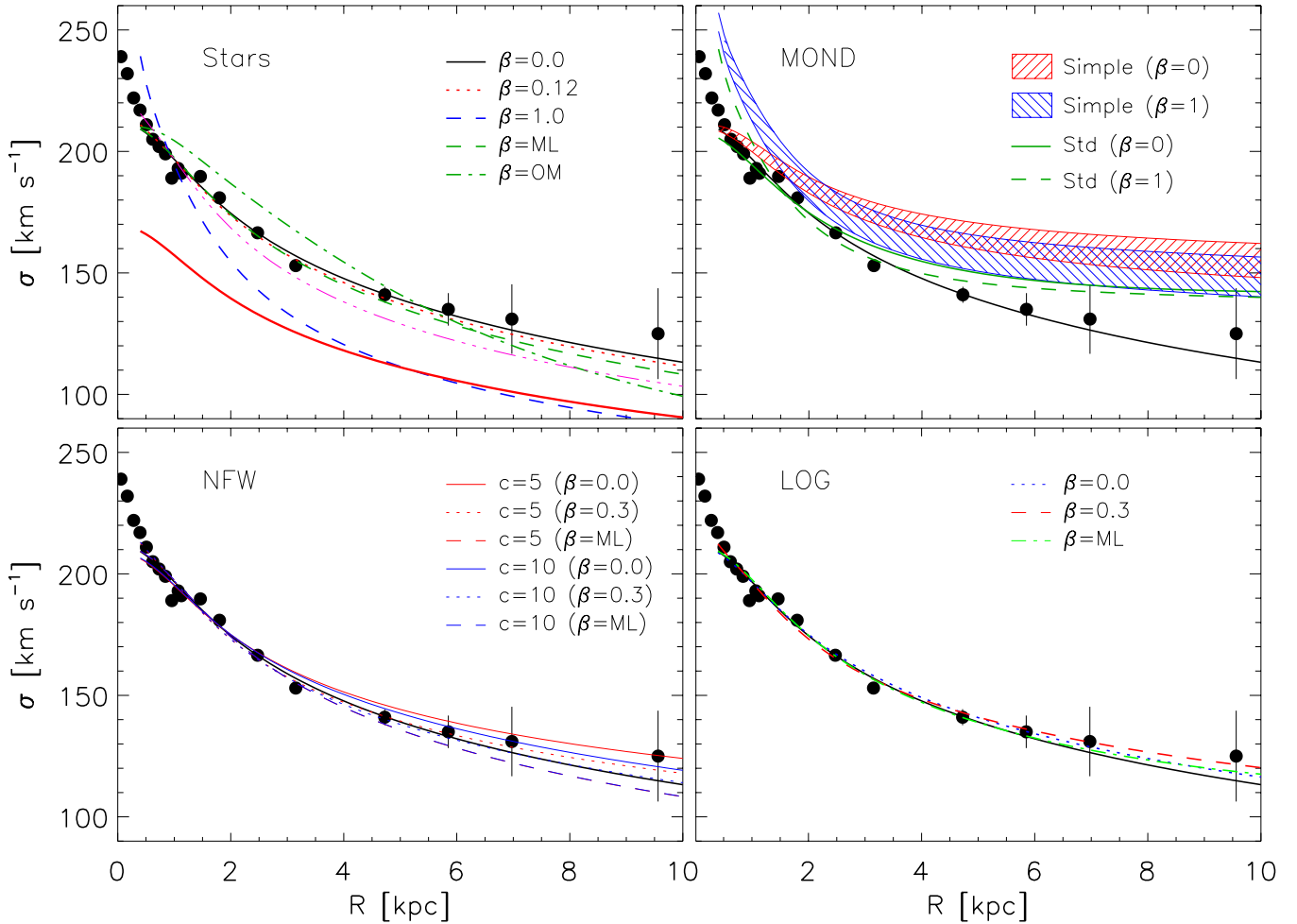


**Fig. 8.** Dynamical models of NGC 7507. Black circles indicate in all panels the line-of-sight velocity dispersion. All models are given outside of 400 pc, where the luminosity model is unaffected by seeing. *Top left:* stars-only models. The black solid line is an isotropic model using  $M/L_R = 3.13$ . This model is shown in all panels as a comparison. The red dotted line is the best-fit model for a constant anisotropy using  $\beta = 0.12$ , while the blue dashed line is a fully radial model ( $\beta = 1$ ). The green dashed line is the model using the anisotropy as given in Eq. (16), while the green dot-dashed line is a model using the Osipkov-Merrit anisotropy (Eq. (17)). The red solid line is a model with  $M/L_R = 2$ , based on Tortora et al.’s stellar population analysis (see Sect. 5.1). *Top right:* MOND predictions using the “simple” and “standard” interpolation formulae. The dashed red area is an isotropic model, while the blue area indicates a fully radial model for the former interpolation. *Bottom left:* NFW models using  $c = 5$  and  $c = 10$ . Parameters for each model are reported in Table 6. *Bottom right:* Logarithmic dark halo models. Using  $\beta = 0$ ,  $\beta = 0.3$ , and ML anisotropy. Parameters for each model are given in Table 7.

**Table 5.** Comparison of different best-fit dynamical models without DM.

Model	$M/L_{\star,R}$ [ $M_{\odot}/L_{\odot,R}$ ]	$\beta$	$\chi^2$
Stars only	$3.13^{+0.01}_{-0.02}$	0.0	46.8
Stars only + cst. $\beta$	$3.11^{+0.02}_{-0.03}$	$0.12^{+0.08}_{-0.08}$	44.1
Stars only + ML <sup>a</sup>	$3.01^{+0.01}_{-0.01}$	0.33	54.5
Stars only + HM <sup>b</sup>	$2.93^{+0.02}_{-0.02}$	0.45	90.5

**Notes.** Errors indicate the  $1-\sigma$  confidence levels. <sup>(a)</sup> Indicates the ML05 anisotropy. The value for  $\beta$  is the maximum value for the anisotropy reached at the last kinematic point. <sup>(b)</sup> Indicates the Hansen & Moore (2006) anisotropy modeled using Eq. (16) with  $r_a = 500$  pc. The value of  $\beta$  has the same meaning as before.

NGC 7507 and calculate for our double-beta model (Eq. (4)) the logarithmic slope  $\alpha = (r/j)dj(r)/dr$ . The resulting anisotropy

profile shows a swift increase from isotropy at the center to  $\beta = 0.3$  at around 500 pc, with a mild increase outwards. This behavior can be reasonably reproduced using the ML05 anisotropy profile with a small  $r_a$ . In the context of a no-DM model, this anisotropy favors an even lower stellar  $M/L$  and underestimates the observed velocity dispersion at large radii, giving a poor fit to the data.

#### 4.5. Including a dark halo

Even though the velocity dispersion profile up to  $\sim 90''$  of NGC 7507 can satisfactorily be described by models without dark matter, the paradigm of galaxy formation requires the presence of dark halos. We therefore allow for a (cuspy) NFW profile (e.g. Navarro et al. 1996) and a (cored) logarithmic halo. In both cases we fix the stellar  $M/L$  to 3.01, therefore maximizing the contribution of the stellar component to the total mass budget (“maximum spheroid”, e.g. Weijmans et al. 2009), this is supported by the fact that the contribution of DM in the inner

**Table 6.** Comparison of different best fitting dynamical models including NFW halos.

$\beta$	$\rho_s$ [ $M_\odot \text{pc}^{-3}$ ]	$r_s$ [kpc]	$r_{200}$ [kpc]	$M_{200}^{\text{DM}}$ [ $M_\odot$ ]	$M(r_{200})/L_R$ [ $M_\odot/L_\odot$ ]	$f_{\text{DM}} < R_e$ [%]	$f_{\text{DM}} < 2R_e$ [%]	$\chi^2$
Stars ( $\Upsilon_R = 3.01$ ) + NFW ( $c = 5$ )								
0.0	$1.191 \times 10^{-3}$	30	150	$3.87^{+3.4}_{-2.1} \times 10^{11}$	7.3	$3.4^{+0.8}_{-0.9}$	$7.5^{+2.5}_{-2.5}$	63.0
0.3	$1.191 \times 10^{-3}$	25	125	$2.24^{+2.0}_{-1.2} \times 10^{11}$	5.6	$2.7^{+0.7}_{-0.8}$	$8.9^{+3.3}_{-3.0}$	40.5
MŁ	$1.191 \times 10^{-3}$	1	5	$1.4^{+1.9} \times 10^7$	3.1	<1	<1	54.5
Stars ( $\Upsilon_R = 3.01$ ) + NFW ( $c = 10$ )								
0.0	$6.135 \times 10^{-3}$	9	90	$8.36^{+6.9}_{-2.5} \times 10^{10}$	4.1	$3.8^{+1.2}_{-0.5}$	$7.1^{+2.9}_{-1.4}$	59.3
0.3	$6.135 \times 10^{-3}$	8	80	$5.87^{+2.5}_{-1.9} \times 10^{10}$	3.8	$3.3^{+0.5}_{-0.6}$	$8.6^{+2.2}_{-1.9}$	42.9
MŁ	$6.135 \times 10^{-3}$	1	10	$0.11^{+7.3} \times 10^9$	3.1	<1	<1	54.5

**Notes.** Column 1 indicates the value for the anisotropy considered for the stellar population. MŁ indicates the Mamon & Łokas (2005b) anisotropy profile with parameters described in the text. Column 2 gives the characteristic density of the NFW halo, which comes from the chosen concentration as given in Eq. (20). Column 3 gives the best fitting scale radius for the chosen concentration. Columns 4 and 5 give the virial radius and mass of the DM halo, respectively. Masses are also indicated with their 1- $\sigma$  confidence level. Column 6 indicates the virial  $M/L$ . Columns 7 and 8 give the DM fraction within 1 and  $2R_e$  (using the effective radius given by Faber et al. 1989), defined as  $f_{\text{DM}} = M_{\text{NFW}}/(M_{\text{NFW}} + M_\star)$ , where the baryonic mass is given by Eq. (6). Column 9 gives the  $\chi^2$  for each model.

regions is thought to be close to negligible (e.g. Gerhard et al. 2001; Borriello et al. 2003; Mamon & Łokas 2005a).

#### 4.5.1. NFW models

The NFW profile is given by

$$\rho_{\text{NFW}}(r) = \frac{\rho_s}{(r/r_s)(1+r/r_s)^2}, \quad (18)$$

where  $\rho_s$  and  $r_s$  are a characteristic density and radius, respectively; the enclosed mass for this profile is given by

$$M_{\text{NFW}}(r) = 4\pi\rho_s r_s^3 \left( \ln(1+r/r_s) - \frac{r/r_s}{1+r/r_s} \right). \quad (19)$$

We explored three models, an isotropic model, a model with a slight radial anisotropy ( $\beta = 0.3$ ) and a model using the MŁ anisotropy with  $r_a = 43''$  as in Sect. 4.4. We excluded the possibility of tangential orbits because they were inconsistent with the stars-only models. For each anisotropy, we used a set of concentrations,  $c = \{1, 1.25, 1.5, \dots, 13\}$ , which encompasses the range of concentrations found for low luminosity ellipticals ( $c \sim 5$ , Napolitano et al. 2008) and the ones found in simulations for halos of similar mass ( $c \sim 10$ , e.g. Bullock et al. 2001; Macciò et al. 2008). Concentrations are related to the characteristic density by

$$\frac{\rho_s}{\rho_{\text{crit}}} = \frac{200}{3} \frac{c^3}{\ln(1+c) - c/(1+c)}, \quad (20)$$

where the critical density is  $\rho_{\text{crit}} = 3H_0^2/8\pi G$ . We also set a grid of characteristic radii,  $r_s = \{1, 2, \dots, 100\}$  kpc, and calculate the  $\chi^2$  for each  $(c, r_s)$  pair. The results can be seen in Fig. 9. 68%, 90% and 99% confidence levels correspond to  $\Delta\chi^2 = \{2.30, 4.61, 9.21\}$  (Avni 1976).

As seen in Fig. 9, we cannot constrain simultaneously  $c$  and  $r_s$ , with the available data/modeling. Even though we have explored a generous range of parameters, a global minimum lies beyond the explored space. The minimum  $\chi^2$  values for the isotropic and MŁ models are worse than the best-fit stars-only models, even though the models with an NFW profile include more free parameters. This is an indication that the data shows a preference for the stars-only models, or more exactly, that our

assumed stellar  $M/L_R$  is closer to the total  $M/L$ , which should be constant across the galaxy. The exception is the model with  $\beta = 0.3$ , which gives a significantly smaller  $\chi^2$  than all of the non-DM models.

Since we cannot constrain simultaneously the values for  $c$  and  $r_s$ , we explore the amount of DM in the NFW halos by selecting the cases  $c = 5$  and  $c = 10$ . The NFW parameters of each halo and the assumed concentrations can be seen in Table 6. The velocity dispersion prediction for each of these models is depicted in Fig. 8 (bottom left panel).

The best-fit model is the one for  $c = 5$  and  $\beta = 0.3$ , which gives a virial mass of  $2.2 \times 10^{11} M_\odot$ . The  $c = 10$  model for the same anisotropy gives a slightly worse fit and a significantly lower virial mass with  $5.9 \times 10^{10} M_\odot$ . Even though the MŁ anisotropy should give a more realistic representation of the true orbital structure of elliptical galaxies, the mass which correspond to the best-fit scale radius is very low, although the 1- $\sigma$  level is broad with a maximum mass of  $1.9 \times 10^{10} M_\odot$  for  $c = 5$ . The Hansen & Moore (2006) anisotropy performs even more poorly, with even lower predicted masses and much larger  $\chi^2$ .

The fraction of DM within  $1R_e$  (using the value from Faber et al. 1989) is lower than 5% for all models. This number can be compared with the values found for galaxies of similar brightness studied by Weijmans et al. (2009): NGC 3379 with  $f_{\text{DM}}(<R_e) = 0.08$  and NGC 821 with  $f_{\text{DM}}(<R_e) = 0.18$ . Even though this low value could be considered as the natural result of the minimal halo assumption, this is not exactly the case. If we were to drop this assumption and allow the stellar  $M/L$  to be a free parameter for the  $c = 5$  and  $c = 10$  NFW halos, we would find that the  $M/L$  diminishes at most to a value of 2.9, depending on the assumed anisotropy, reinforcing the prior assumption. DM fractions within  $2R_e$  can also be seen in Table 6.

#### 4.5.2. Models with a logarithmic halo

Even though most, if not all,  $N$ -body simulations favor cuspy profiles, observations of dwarf and low surface brightness galaxies indicate the presence of constant density cores instead of  $r^{-1}$  cusps (see de Blok 2010, for a recent review). From the

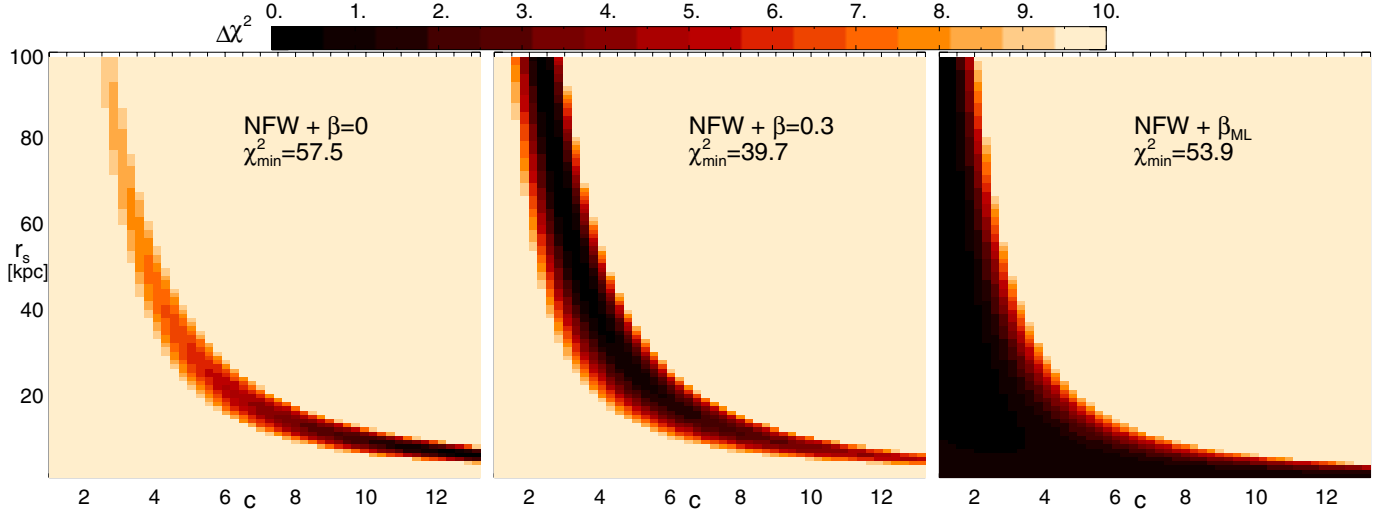


**Fig. 9.**  $\chi^2$  for models including an NFW halo. Minimum  $\chi^2$  for each model is indicated. *Left panel:* NFW halo and stars with isotropic distribution. *Central panel:* NFW halo plus stars with a radial anisotropy of  $\beta=0.3$ . *Right panel:* NFW halo and stars following a M $\dot{L}$  anisotropy profile.

different types of cored profiles, we selected the logarithmic potential (Binney & Tremaine 2008), which has a density

$$\rho_{\text{LOG}}(r) = \frac{v_0^2}{4\pi G} \frac{3r_0^2 + r^2}{(r_0^2 + r^2)^2}, \quad (21)$$

and enclosed mass

$$M_{\text{LOG}}(r) = \frac{v_0^2 r}{G \left(1 + \left(\frac{r_0}{r}\right)^2\right)}. \quad (22)$$

The modeling procedure is similar to the one applied in the section. As for the NFW profiles, the stellar  $M/L_R$  remains fixed at 3.01. A grid of parameters was then set with  $r_0 = \{1, 2, \dots, 80\}$  kpc and  $v_0 = \{40, 45, \dots, 215\}$  km s $^{-1}$  and for each pair, the value of  $\chi^2$  is calculated using Eq. (15) for the same three anisotropies as in the previous section;  $\beta=0$ ,  $\beta=0.3$ , and  $\beta(r)$  following Eq. (16). The grid was later refined for the case  $\beta=0$ . The best-fitting halo parameters for each studied case are given in Table 7.

The isotropic case allows a light halo with a very small characteristic radius of only 25 pc. Assuming  $\beta=0.3$  the halo is much larger with  $r_0 = 7$  kpc and a circular velocity of 100 km s $^{-1}$ . This radial model provides a significantly tighter fit to the observed velocity dispersion. This halo is the one that gives the lowest  $\chi^2$  amongst all models (with or without DM). The M $\dot{L}$  anisotropy allows a large range of possible halos, but giving a worse fit than the  $\beta=0.3$  case. As in the case of NFW halos, the amount of DM enclosed within one  $R_e$  is minimal, again having values of less than 5% for all models. The velocity dispersion for these three best-fit models can be seen in Fig. 8 (bottom right panel).

#### 4.6. The Gauss-Hermite parameter $h_4$

Predictions for the Gauss-Hermite  $h_4$  profile for different models can be seen in Fig. 10, where we have followed the procedure of Łokas (2002) and related kurtosis and  $h_4$  using

$$\kappa(R) \simeq 8 \sqrt{6} h_4, \quad (23)$$

(van der Marel & Franx 1993). We have considered the stars-only, NFW with  $c = 5$  and 10, and the logarithmic cases with isotropy and completely radial anisotropies. Although

**Table 7.** Comparison of different best-fit dynamical models using a logarithmic DM halo.

$\beta$	$r_0$ [pc]	$v_0$ km s $^{-1}$	$f_{\text{DM}} < R_e$ [%]	$f_{\text{DM}} < 2R_e$ [%]	$\chi^2$
0.0	25	60	4.1	5.4	47.7
0.3	7000	100	2.3	7.4	38.6
M $\dot{L}$	74 000	210	<1	<1	52.4

**Notes.** All models use  $M/L_{\star,R} = 3$ .

the velocity dispersion profiles are best reproduced with radial anisotropies using  $\beta=0.3$ , we did not calculate their  $h_4$  predictions since they would lie between the two aforementioned models, without adding new information. As in the cases of the velocity dispersion profiles, since the light profile is affected by seeing, the model is not expected to reproduce the inner 400 pc.

The measured  $h_4$  data are noisy (green circles) and all models systematically fail to reproduce its high values. We note that the K+00 data are equally noisy and reach similar high values (blue stars in Fig. 10). The difference is most evident in the inner 500 pc where the K+00 values are closer to zero and ours scatter around  $\sim 0.05$ . Although some systematic effect may be shifting our measurements to higher values, it can hardly be  $S/N$  (which is especially high at small radii) nor template mismatching (innermost spectra are very well-fitted using the comprehensive MILES stellar library). Perhaps the only conclusion that we can give is that the  $h_4$  data does not favor isotropic models, which predict slightly negative values for  $h_4$  (see Sect. 5.3 for an alternative explanation).

## 5. Discussion

### 5.1. Stellar $M/L$

The stellar  $M/L$  determines the amount of baryonic matter and thus, based on its difference from the total mass, also the fraction of dark matter. Our  $M/L$ -value is not quite consistent with what one would theoretically expect for an old, metal-rich population by comparison with published population synthesis models, but it is in agreement with literature values.

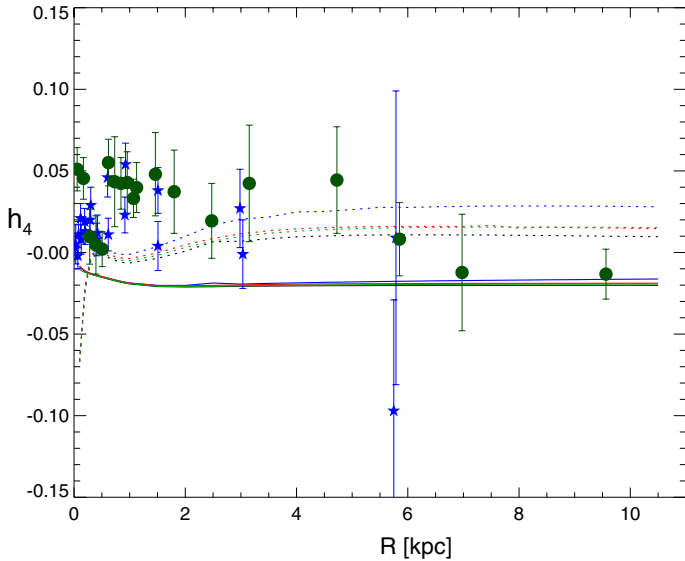


**Fig. 10.** Kurtosis models for NGC 7507. Green circles represent our  $h_4$  measurements as given in Table 4. Blue stars are the measurements from K+00. Black, red, blue, and green lines represent the stars-only, NFW ( $c = 5$ ), NFW ( $c = 10$ ), and logarithmic models, with parameters described in the text, respectively. Solid lines are isotropic models, while dotted lines are fully radial models.

K+00 gives a central  $M/L_B$  value of 5.9 for a distance of 26.9 Mpc. Since dynamically derived  $M/L$ s are inversely proportional to distance, at our adopted distance of 23.2 Mpc this value transforms into  $M/L_B = 6.8$ , which gives  $M/L_R = 3.14$  using  $(B-R) = 1.90$  (Franx et al. 1989b) and  $(B-R)_\odot = 1.06$  (Binney & Merrifield 1998), in excellent agreement with our value. Magorrian & Ballantyne (2001), based on kinematic data by Bertin et al. (1994), found  $M/L_B \sim 7$ , somewhat higher than our value, but also in agreement considering their shorter distance (21 Mpc).

The stellar  $M/L$ s even of old elliptical galaxies are apparently not universal: Cappellari et al. (2006) find values in the range  $1.5 \lesssim M/L_I \lesssim 6.0$ . For NGC 7507,  $M/L_R = 3.1$  translates into  $M/L_I = 2.42$ . If we only consider elliptical galaxies in the Cappellari et al. (2006) sample, that is, excluding S0 galaxies, this range would narrow to  $2.3 \lesssim M/L_I \lesssim 6.1$ , putting NGC 7507 among the ellipticals with the lowest  $M/L$ . This value, unless the metal abundance of NGC 7507 is distinctly subsolar, would indicate a somewhat younger galaxy, with an age around 8 Gyr for a solar abundance, which agrees with previous line-strength measurements of this galaxy (Trager et al. 1998; Ogando et al. 2008). This is unsurprising because a large fraction of isolated elliptical galaxies are known to be of younger age (Collobert et al. 2006; Reda et al. 2007), which is consistent also with simulations (Niemi et al. 2010). Tortora et al.’s (2009) stellar population models give a very similar age of 7.7 Gyr (Kroupa IMF), but a significantly different  $M/L_R = 2$ . This value is in contradiction with the line strength analyses and with our dynamically derived  $M/L$  and would imply a huge DM content, even in the innermost parts of the galaxy (red solid line in Fig. 8, top left panel).

## 5.2. Dark matter?

That an isotropic model with no DM closely fits the observations nicely, does not imply that there is no DM. This situation was realized before in analyses where PNe were used

as dynamical tracers (Romanowsky et al. 2003; Dekel et al. 2005, MŁ05). However, the relatively low stellar  $M/L$ -value of NGC 7507 is in line with the finding that, regardless of the situation at larger radii, the DM content in the inner region of elliptical galaxies is negligible (Gerhard et al. 2001; Mamon & Łokas 2005a; Cappellari et al. 2006). Within the framework of a spherical model, a possibility to host DM at larger radii is a radial anisotropy. It must then be a coincidence that the observed dispersion so closely follows the predictions of the photometric model under isotropy. This is a difference to the use of PNe as dynamical tracers, where the density profile of the parent population is notoriously uncertain.

Are the stellar orbits of NGC 7507 affected by a strong radial anisotropy? The comparison with the kurtosis profiles for a few models shows that a fully radial anisotropy of the stellar component can produce a consistently positive kurtosis of the observed order, although failing in the innermost regions. However, we say that with caution, since the kurtosis might also be influenced by rotation (Dekel et al. 2005).

NGC 7507 with a stellar mass of about  $2 \times 10^{11} M_\odot$  belongs to the most massive isolated elliptical galaxies in the simulations of Niemi et al. (2010). The dark halos in which they are embedded have predicted masses of the order of a few times  $10^{12} M_\odot$  within their virial radii. Our halos from Table 6 are far from this mass, although we caution that the extrapolation to the virial radius might be uncertain (Mamon & Łokas 2005b).

## 5.3. Limitations of a spherical model

Even though the apparent spherical symmetry of the galaxy and the small amount of rotation give reasons to use our modeling approach, at the same time other observations may point to a more complex scenario. High  $h_4$  values could be signature of an undetected face-on disk or flattening along the line of sight (Magorrian 1999; Magorrian & Ballantyne 2001), which might also explain the failure to reproduce the  $h_4$  values when using the Łokas (2002) simplification. The second observed particularity is the rotation along the minor axis. Elliptical galaxies with this property are rare: Franx et al. (1989b) found that minor axis rotation was larger than major axis rotation in only 2 out of 22 galaxies in their sample. This behavior is a signature of triaxial galaxies (e.g. Binney 1985). Another sign of triaxiality comes from the outermost velocity along the major axis which shows a significant difference with the inner measurements. This change in the mean velocity corresponds to a sudden change in the ellipticity at the same radius ( $\sim 100''$ , Figs. 2 and 5).

## 5.4. MOND and the baryonic Tully-Fisher relation

Among the problems that MOND faces is how the Newtonian and MONDian regimes are linked. Taking this interpolation function as  $\mu(x) = x/(1+x)$  (known as “simple”, Famaey & Binney 2005), the MONDian circular velocity is

$$v_{\text{circ,MOND}}^2(r) = \frac{v_{\text{circ,N}}^2}{2} + \sqrt{\frac{v_{\text{circ,N}}^4}{4} + a_0 v_{\text{circ,N}}^2 r} \quad (24)$$

(e.g. Richtler et al. 2008), where  $v_{\text{circ,N}}$  is the Newtonian circular velocity associated with the stellar component and  $a_0 = 1.35^{+0.28}_{-0.42} \times 10^{-8} \text{ cm s}^{-2}$  (Famaey et al. 2007) is the acceleration constant that separates the MOND and Newtonian realms. An alternative interpolation function, dubbed “standard”, is

$\mu(x) = x / \sqrt{1 + x^2}$  (Sanders & McGaugh 2002), for which the circular velocity is given by

$$v_{\text{circ,MOND}}^4(r) = \frac{v_{\text{circ,N}}^4}{2} + \sqrt{\frac{v_{\text{circ,N}}^8}{4} + a_0^2 v_{\text{circ,N}}^4 r^2} \quad (25)$$

(e.g. Samurović & Ćirković 2008). The masses associated with these circular velocities are introduced in Eq. (14) to obtain the MOND predictions for the projected velocity dispersion profile for the isotropic case, using in all cases  $M/L_{\star,R} = 3$ . As seen in Fig. 8 (top right panel), the simple interpolation formula cannot explain the velocity dispersion profile under isotropy. The outermost measured points can only be explained under a totally radial model and only when the lowest allowed values for  $a_0$  are considered. The standard interpolation formula (green lines in the same plot) gives very similar predictions for the isotropic and radial cases for the outermost bins, and again favors a lower value for  $a_0$ .

The barred spiral galaxy NGC 7513 is found at an angular distance of 18.2 arcmin from NGC 7507. In the MOND context, it is interesting to ask whether it could provide an external gravitational field which would modify the MOND phenomenology in NGC 7507. The mean of the published Tully-Fisher distances is 19.3 Mpc and thus places NGC 7513 with respect to NGC 7507 (23 Mpc) somewhat in the foreground and a separation of 4 Mpc would produce a very weak field. Adopting an inclination-corrected HI-line width of  $275 \text{ km s}^{-1}$  as the value for a constant MONDian rotation curve (Springob et al. 2007), the acceleration at NGC 7507 would be  $6.3 \times 10^{-13} \text{ m s}^{-2}$ . Assuming the same distance as for NGC 7507, the separation would be 123 kpc and the acceleration at NGC 7507 would be  $2 \times 10^{-11} \text{ m s}^{-2}$ . Therefore, an external field should not influence any of the MONDian dynamics of NGC 7507.

The baryonic Tully-Fisher relation (BTFR) of spiral galaxies relates circular velocity (which is a proxy for the *total* mass) to the *baryonic* content of the galaxy. This relation, which reads  $M_{\text{bar}} = 50 v_f^4$ , where  $v_f$  is the circular velocity in the flat part of the rotation curve, has been found to be correct over many orders of magnitude (McGaugh 2005; Trachternach et al. 2009). A tight relation between baryonic mass and circular velocities is not expected when DM is assumed to dominate the dynamics, but it finds a natural explanation under MOND (Sanders & McGaugh 2002). Similarly to spirals, early-type galaxies have been found to follow a relation that is analogous to the Tully-Fisher relation (Gerhard et al. 2001; Magorrian & Ballantyne 2001), but since circular velocities up to a large radius are difficult to obtain, there is no surprise in finding that ellipticals follow a relation that is offset from the spiral BTFR, i.e. circular velocities are probably overestimated. For NGC 7507, we calculated the circular velocity at the outermost point with measured kinematics of  $250 \text{ km s}^{-1}$ . Using McGaugh's version of the BTFR, this implies a mass of  $2 \times 10^{11} M_{\odot}$ . Using Eq. (6) with our preferred  $M/L$  value, we obtained  $2.5 \times 10^{11} M_{\odot}$ , that is, NGC 7507 would lie somewhat above the BTFR for spirals; this appears inconsistent with previous results for other ellipticals (Gerhard et al. 2001), although consistent when all uncertainties are taken into account. We also note that the slope of 4 required by MOND remains a disputed value (see e.g. Gurovich et al. 2010).

## 6. Summary and conclusions

We have obtained wide-field photometry in Kron-Cousins  $R$  and Washington  $C$  as well as new long-slit spectroscopy of the field

elliptical NGC 7507 out to about  $\sim 90''$ , reaching farther out than previous studies.

We have measured almost no rotation along the major axis and significant rotation ( $\Delta v \sim 50 \text{ km s}^{-1}$ ) along the minor axis (although the galaxy is almost perfectly circular). The velocity dispersion profile of the galaxy shows a rapid decline along both axes.

We have performed a spherical Jeans analysis to find the mass profile that most closely represents the projected velocity dispersion profile. When assuming isotropy, a radially constant  $M/L_R$  ratio of 3.1 would be sufficient to reproduce the velocity dispersions. This value corresponds, if solar abundance is assumed, to an age in the range 8–10 Gyr. DM halos can be included in the isotropic case, but provide significantly poorer fits than the stars-only models. When we allowed for radial anisotropies and cored/cuspy dark halos, we were able to improve the fit to the velocity dispersion profile marginally. This contradicts the result of Kronawitter et al. (2000) and Gerhard et al. (2001) who found this galaxy to be one of the best examples for hosting a dark halo. It is however in line with the results of Magorrian & Ballantyne (2001) who also found no clear evidence of DM.

The most massive NFW halo, using  $\beta = 0.3$  and a concentration parameter of 5, has a scale  $r_s = 25 \text{ kpc}$ , implying a virial mass of only  $2.2_{-1.2}^{+2.1} \times 10^{11} M_{\odot}$ . Modified Newtonian dynamics (MOND), if applied straightforwardly, predicts velocity dispersions that are too high.

It appears that NGC 7507 is a very interesting case in the discussion of DM in elliptical galaxies. It remains to be seen whether non-spherical models based on an extended data set, perhaps including also PNe and/or globular clusters, would provide different results.

*Acknowledgements.* We thank the referee, Dr. Gary Mamon, for a careful and insightful report. We thank Roberto Saglia for providing the kinematic measurements from Kronawitter et al. (2000) in electronic form. We thank Srđjan Samurović and Michael Hilker for making available their Linux compatible versions of R. van der Marel's code; Michele Cappellari and Anne-Marie Weijmans for useful advice on the usage of pPXF. R.S. acknowledges support from a CONICYT doctoral fellowship and the ESO Studentship Program. T.R. acknowledges support from the Chilean Center for Astrophysics, FONDAF Nr. 15010003, and from FONDECYT project Nr. 1100620. L.P.B. acknowledges support from CONICET, Agencia Nacional de Promoción Científica y Tecnológica, and Universidad Nacional de La Plata (Argentina). A.J.R. was supported by National Science Foundation grants AST-0808099 and AST-0909237.

## References

- Abadi, M. G., Navarro, J. F., & Steinmetz, M. 2006, MNRAS, 365, 747  
Avni, Y. 1976, ApJ, 210, 642  
Bedregal, A. G., Aragón-Salamanca, A., Merrifield, M. R., & Milvang-Jensen, B. 2006, MNRAS, 371, 1912  
Beers, T. C., Flynn, K., & Gebhardt, K. 1990, AJ, 100, 32  
Beifiori, A., Maraston, C., Thomas, D., & Johansson, J. 2011, A&A, 531, A109  
Bertin, G., Bertola, F., Buson, L. M., et al. 1994, A&A, 292, 381  
Binney, J. 1985, MNRAS, 212, 767  
Binney, J., & Mamon, G. A. 1982, MNRAS, 200, 361  
Binney, J., & Merrifield, M. 1998, Galactic Astronomy (Princeton University Press)  
Binney, J., & Tremaine, S. 2008, Galactic Dynamics, second edition (Princeton University Press)  
Borriello, A., Salucci, P., & Danese, L. 2003, MNRAS, 341, 1109  
Bullock, J. S., Kolatt, T. S., Sigad, Y., et al. 2001, MNRAS, 321, 559  
Cappellari, M., & Emsellem, E. 2004, PASP, 116, 138  
Cappellari, M., Bacon, R., Bureau, M., et al. 2006, MNRAS, 366, 1126  
Cappellari, M., Emsellem, E., Bacon, R., et al. 2007, MNRAS, 379, 418  
Cocato, L., Gerhard, O., Arnaboldi, M., et al. 2009, MNRAS, 394, 1249  
Collobert, M., Sarzi, M., Davies, R. L., Kuntschner, H., & Colless, M. 2006, MNRAS, 370, 1213  
de Blok, W. J. G. 2010, Adv. Astron., 2010, 5

- de Lorenzi, F., Gerhard, O., Coccatto, L., et al. 2009, *MNRAS*, 395, 76
- de Souza, R. E., Gadotti, D. A., & dos Anjos, S. 2004, *ApJS*, 153, 411
- de Vaucouleurs, G., de Vaucouleurs, A., & Corwin, J. R. 1976, in *Second reference catalogue of bright galaxies* (Austin: University of Texas Press), 0
- Dekel, A., Stoehr, F., Mamon, G. A., et al. 2005, *Nature*, 437, 707
- Dirsch, B., Richtler, T., Geisler, D., et al. 2003, *AJ*, 125, 1908
- Dirsch, B., Schuberth, Y., & Richtler, T. 2005, *A&A*, 433, 43
- Doherty, M., Arnaboldi, M., Das, P., et al. 2009, *A&A*, 502, 771
- Douglas, N. G., Napolitano, N. R., Romanowsky, A. J., et al. 2007, *ApJ*, 664, 257
- Emsellem, E., Cappellari, M., Krajnović, D., et al. 2007, *MNRAS*, 379, 401
- Faber, S. M., Wegner, G., Burstein, D., et al. 1989, *ApJS*, 69, 763
- Famaey, B., & Binney, J. 2005, *MNRAS*, 363, 603
- Famaey, B., Gentile, G., Bruneton, J., & Zhao, H. 2007, *Phys. Rev. D*, 75, 063002
- Forestell, A. D., & Gebhardt, K. 2010, *ApJ*, 716, 370
- Franx, M., Illingworth, G., & Heckman, T. 1989a, *ApJ*, 344, 613
- Franx, M., Illingworth, G., & Heckman, T. 1989b, *AJ*, 98, 538
- Geisler, D. 1996, *AJ*, 111, 480
- Gerhard, O. E. 1993, *MNRAS*, 265, 213
- Gerhard, O., Kronawitter, A., Saglia, R. P., & Bender, R. 2001, *AJ*, 121, 1936
- Goudfrooij, P., Hansen, L., Jorgensen, H. E., et al. 1994, *A&AS*, 104, 179
- Graham, A. W., & Driver, S. P. 2005, *PASA*, 22, 118
- Gurovich, S., Freeman, K., Jerjen, H., Staveley-Smith, L., & Puerari, I. 2010, *AJ*, 140, 663
- Hansen, S. H., & Moore, B. 2006, *New A*, 11, 333
- Jensen, J. B., Tonry, J. L., Barris, B. J., et al. 2003, *ApJ*, 583, 712
- Kelson, D. D., Zabludoff, A. I., Williams, K. A., et al. 2002, *ApJ*, 576, 720
- Kronawitter, A., Saglia, R. P., Gerhard, O., & Bender, R. 2000, *A&AS*, 144, 53
- Lauberts, A., & Valentijn, E. A. 1989, *The surface photometry catalogue of the ESO-Uppsala galaxies*
- Lima Neto, G. B., Gerbal, D., & Márquez, I. 1999, *MNRAS*, 309, 481
- Łokas, E. L. 2002, *MNRAS*, 333, 697
- Macciò, A. V., Dutton, A. A., & van den Bosch, F. C. 2008, *MNRAS*, 391, 1940
- Magorrian, J. 1999, *MNRAS*, 302, 530
- Magorrian, J., & Ballantyne, D. 2001, *MNRAS*, 322, 702
- Mamon, G. A., & Łokas, E. L. 2005a, *MNRAS*, 362, 95
- Mamon, G. A., & Łokas, E. L. 2005b, *MNRAS*, 363, 705
- Mamon, G. A., Łokas, E., Dekel, A., Stoehr, F., & Cox, T. J. 2006, in *EAS Pub. Ser. 20*, ed. G. A. Mamon, F. Combes, C. Deffayet, & B. Fort, 139
- McGaugh, S. S. 2005, *ApJ*, 632, 859
- Méndez, R. H., Teodorescu, A. M., Kudritzki, R.-P., & Burkert, A. 2009, *ApJ*, 691, 228
- Merritt, D. 1985, *MNRAS*, 214, 25P
- Milgrom, M. 1983, *ApJ*, 270, 365
- Napolitano, N. R., Romanowsky, A. J., Coccatto, L., et al. 2008, in *IAU Symp. 244*, ed. J. Davies, & M. Disney, 289
- Napolitano, N. R., Romanowsky, A. J., Coccatto, L., et al. 2009, *MNRAS*, 393, 329
- Napolitano, N. R., Romanowsky, A. J., Capaccioli, M., et al. 2010, *MNRAS*, 1835
- Navarro, J. F., Frenk, C. S., & White, S. D. M. 1996, *ApJ*, 462, 563
- Niemi, S., Heinämäki, P., Nurmi, P., & Saar, E. 2010, *MNRAS*, 405, 477
- Ogando, R. L. C., Maia, M. A. G., Pellegrini, P. S., & da Costa, L. N. 2008, *AJ*, 135, 2424
- Osipkov, L. P. 1979, *Soviet Astron. Lett.*, 5, 42
- Poulain, P., & Nieto, J.-L. 1994, *A&AS*, 103, 573
- Proctor, R. N., Forbes, D. A., Romanowsky, A. J., et al. 2009, *MNRAS*, 398, 91
- Prugniel, P., & Simien, F. 1997, *A&A*, 321, 111
- Pu, S. B., Saglia, R. P., Fabricius, M. H., et al. 2010, *A&A*, 516, A4
- Reda, F. M., Proctor, R. N., Forbes, D. A., Hau, G. K. T., & Larsen, S. S. 2007, *MNRAS*, 377, 1772
- Richtler, T., Schuberth, Y., Hilker, M., et al. 2008, *A&A*, 478, L23
- Richtler, T., Salinas, R., Misgeld, I., et al. 2011, *A&A*, 531, A119
- Romanowsky, A. J., Douglas, N. G., Arnaboldi, M., et al. 2003, *Science*, 301, 1696
- Romanowsky, A. J., Strader, J., Spitler, L. R., et al. 2009, *AJ*, 137, 4956
- Samurović, S., & Čirković, M. M. 2008, *A&A*, 488, 873
- Samurović, S., & Danziger, I. J. 2005, *MNRAS*, 363, 769
- Sánchez-Blázquez, P., Peletier, R. F., Jiménez-Vicente, J., et al. 2006, *MNRAS*, 371, 703
- Sanders, R. H., & McGaugh, S. S. 2002, *ARA&A*, 40, 263
- Schlegel, D. J., Finkbeiner, D. P., & Davis, M. 1998, *ApJ*, 500, 525
- Schuberth, Y., Richtler, T., Dirsch, B., et al. 2006, *A&A*, 459, 391
- Schuberth, Y., Richtler, T., Hilker, M., et al. 2010, *A&A*, 513, A52
- Sersic, J. L. 1968, *Atlas de galaxias australes*, ed. J. L. Sersic
- Shapiro, K. L., Cappellari, M., de Zeeuw, T., et al. 2006, *MNRAS*, 370, 559
- Springob, C. M., Masters, K. L., Haynes, M. P., Giovanelli, R., & Marinoni, C. 2007, *ApJS*, 172, 599
- Statler, T. S., & Smecker-Hane, T. 1999, *AJ*, 117, 839
- Stetson, P. B. 1987, *PASP*, 99, 191
- Tal, T., van Dokkum, P. G., Nelan, J., & Bezanson, R. 2009, *AJ*, 138, 1417
- Teodorescu, A. M., Méndez, R. H., Bernardi, F., Riffeser, A., & Kudritzki, R. P. 2010, *ApJ*, 721, 369
- Thomas, J., Saglia, R. P., Bender, R., et al. 2007, *MNRAS*, 382, 657
- Tonry, J. L., Dressler, A., Blakeslee, J. P., et al. 2001, *ApJ*, 546, 681
- Tortora, C., Napolitano, N. R., Romanowsky, A. J., Capaccioli, M., & Covone, G. 2009, *MNRAS*, 396, 1132
- Trachternach, C., de Blok, W. J. G., McGaugh, S. S., van der Hulst, J. M., & Dettmar, R. 2009, *A&A*, 505, 577
- Trager, S. C., Worthey, G., Faber, S. M., Burstein, D., & Gonzalez, J. J. 1998, *ApJS*, 116, 1
- van der Marel, R. P. 1994, *MNRAS*, 270, 271
- van der Marel, R. P., & Franx, M. 1993, *ApJ*, 407, 525
- Vazdekis, A., Sánchez-Blázquez, P., Falcón-Barroso, J., et al. 2010, *MNRAS*, 404, 1639
- Weijmans, A.-M., Cappellari, M., Bacon, R., et al. 2009, *MNRAS*, 1006
- Wu, X., Zhao, H., Famaey, B., et al. 2007, *ApJ*, 665, L101

**Table 1.**  $T1$  CTIO/MOSAIC surface photometry of NGC 7507.

$R$ (arcsec)	$\mu_{T1}$ (mag arcsec $^{-2}$ )	$\epsilon$	$a_4$	PA
0.148	15.136 ± 0.001	0.264	0.104 ± 0.043	-23.9 ± 8.4
0.511	15.186 ± 0.001	0.052	-0.023 ± 0.011	-33.6 ± 16.3
1.095	15.550 ± 0.001	0.031	-0.003 ± 0.001	8.3 ± 3.4
1.457	15.797 ± 0.001	0.033	-0.001 ± 0.001	8.8 ± 2.1
2.133	16.194 ± 0.001	0.040	-0.001 ± 0.001	13.8 ± 1.5
2.581	16.424 ± 0.001	0.043	-0.001 ± 0.001	12.8 ± 1.3
3.123	16.678 ± 0.001	0.040	-0.002 ± 0.001	15.4 ± 1.0
3.435	16.810 ± 0.001	0.039	-0.001 ± 0.001	16.3 ± 1.2
4.572	17.200 ± 0.001	0.046	-0.000 ± 0.001	14.4 ± 1.1
5.029	17.326 ± 0.001	0.048	-0.000 ± 0.001	16.4 ± 0.8
5.532	17.449 ± 0.002	0.052	-0.001 ± 0.001	15.1 ± 1.1
6.086	17.574 ± 0.002	0.054	-0.002 ± 0.001	15.7 ± 0.9
7.364	17.837 ± 0.002	0.054	0.003 ± 0.001	15.6 ± 0.8
8.100	17.983 ± 0.003	0.050	0.001 ± 0.001	16.7 ± 0.8
8.910	18.138 ± 0.003	0.046	0.001 ± 0.001	14.7 ± 0.9
9.801	18.307 ± 0.004	0.042	-0.001 ± 0.001	15.5 ± 0.9
10.782	18.475 ± 0.001	0.042	0.002 ± 0.001	12.1 ± 0.5
11.860	18.646 ± 0.001	0.042	0.002 ± 0.001	12.1 ± 0.5
13.046	18.817 ± 0.001	0.042	0.003 ± 0.001	12.1 ± 0.5
14.351	18.985 ± 0.001	0.042	0.003 ± 0.001	12.1 ± 0.6
15.786	19.145 ± 0.001	0.045	0.002 ± 0.001	13.0 ± 0.5
17.364	19.302 ± 0.001	0.048	0.001 ± 0.001	11.8 ± 0.5
19.101	19.468 ± 0.002	0.043	0.004 ± 0.001	10.3 ± 0.6
21.011	19.621 ± 0.002	0.045	0.003 ± 0.001	10.3 ± 0.5
23.112	19.772 ± 0.002	0.047	0.003 ± 0.001	8.4 ± 0.5
25.423	19.928 ± 0.003	0.046	0.002 ± 0.001	9.2 ± 0.5
27.965	20.096 ± 0.003	0.044	0.001 ± 0.001	10.3 ± 0.4
30.762	20.278 ± 0.003	0.043	-0.001 ± 0.001	12.0 ± 0.4
33.838	20.473 ± 0.004	0.044	0.000 ± 0.001	11.9 ± 0.4
37.221	20.682 ± 0.005	0.040	-0.000 ± 0.001	14.7 ± 0.5
40.944	20.894 ± 0.006	0.039	-0.001 ± 0.001	16.5 ± 0.6
45.038	21.116 ± 0.008	0.037	-0.002 ± 0.001	16.6 ± 0.7
49.542	21.336 ± 0.009	0.040	-0.001 ± 0.001	17.2 ± 0.7
54.496	21.539 ± 0.011	0.041	-0.001 ± 0.001	18.4 ± 0.8
59.946	21.736 ± 0.013	0.044	-0.002 ± 0.001	19.9 ± 0.9
65.940	21.934 ± 0.016	0.040	0.000 ± 0.001	26.4 ± 1.0
72.534	22.138 ± 0.019	0.043	-0.002 ± 0.001	23.1 ± 1.1
79.788	22.328 ± 0.023	0.048	-0.004 ± 0.001	23.8 ± 1.1
87.766	22.541 ± 0.028	0.043	-0.003 ± 0.001	25.3 ± 1.5
96.543	22.729 ± 0.034	0.045	-0.005 ± 0.001	23.9 ± 1.7
106.197	22.894 ± 0.039	0.069	-0.002 ± 0.002	28.2 ± 1.5
116.817	23.031 ± 0.045	0.081	0.002 ± 0.002	30.4 ± 1.3
128.499	23.177 ± 0.051	0.081	0.009 ± 0.002	37.7 ± 1.3
141.349	23.329 ± 0.059	0.081	0.000 ± 0.002	35.4 ± 1.3
155.484	23.490 ± 0.069	0.097	-0.010 ± 0.002	28.5 ± 1.1
171.032	23.689 ± 0.083	0.100	-0.000 ± 0.002	26.0 ± 1.3
188.135	23.900 ± 0.102	0.088	-0.019 ± 0.003	28.4 ± 1.7
206.949	24.076 ± 0.121	0.115	-0.028 ± 0.003	29.9 ± 1.1
227.643	24.381 ± 0.164	0.098	-0.021 ± 0.003	34.7 ± 1.7
250.408	24.611 ± 0.207	0.113	-0.020 ± 0.004	38.4 ± 1.7
275.449	24.842 ± 0.262	0.121	0.002 ± 0.004	36.4 ± 1.9
302.993	25.102 ± 0.346	0.121	-0.087 ± 0.015	45.0 ± 3.9
333.293	25.318 ± 0.439	0.121	-0.029 ± 0.007	38.1 ± 2.6
366.622	25.566 ± 0.589	0.121	-0.001 ± 0.008	38.1 ± 3.6
403.284	25.849 ± 0.854	0.121	0.009 ± 0.009	38.1 ± 3.9
443.613	26.128 ± 1.324	0.121	0.027 ± 0.011	38.1 ± 4.3
487.974	26.428 ± 2.893	0.121	0.069 ± 0.056	38.1 ± 4.8

**Notes.** First column indicates the semi-major axis from the ellipse fitting.

**Table 2.** Major axis kinematics of NGC 7507.

$R$ (arcsec)	$v_{\text{rot}}$ ( $\text{km s}^{-1}$ )	$\sigma_V$ ( $\text{km s}^{-1}$ )	$h_3$	$h_4$
-32.78	4.4 ± 4.8	124.1 ± 6.6	-0.065 ± 0.027	0.051 ± 0.017
-28.68	1.5 ± 5.7	144.2 ± 7.0	-0.001 ± 0.028	0.032 ± 0.020
-25.51	-1.5 ± 5.7	155.1 ± 7.2	-0.001 ± 0.028	0.025 ± 0.022
-22.96	-2.5 ± 6.4	158.7 ± 7.2	0.016 ± 0.028	-0.003 ± 0.025
-20.78	-11.8 ± 5.7	164.4 ± 6.9	0.043 ± 0.026	0.011 ± 0.026
-18.88	3.5 ± 5.8	164.3 ± 8.6	-0.007 ± 0.027	0.057 ± 0.025
-17.28	-9.4 ± 6.3	189.6 ± 8.6	0.007 ± 0.024	0.047 ± 0.025
-15.90	4 ± 5.8	175.6 ± 7.9	-0.033 ± 0.025	0.048 ± 0.022
-14.66	-5.8 ± 6.7	189.8 ± 7.9	-0.002 ± 0.024	0.018 ± 0.025
-13.57	9 ± 6.9	187.9 ± 7.9	-0.010 ± 0.024	0.039 ± 0.024
-12.62	-3.3 ± 6.0	193.7 ± 8.6	0.012 ± 0.023	0.046 ± 0.023
-11.82	1.2 ± 6.5	196.9 ± 8.2	0.012 ± 0.025	0.015 ± 0.023
-11.09	-4.4 ± 7.6	192.1 ± 8.1	-0.007 ± 0.024	0.021 ± 0.026
-10.43	-3.1 ± 6.9	196.3 ± 8.5	-0.015 ± 0.024	0.025 ± 0.024
-9.85	-3.4 ± 6.1	187.1 ± 8.2	-0.007 ± 0.023	0.036 ± 0.023
-9.26	-8.8 ± 5.8	197.2 ± 7.9	-0.000 ± 0.022	0.018 ± 0.023
-8.75	-2.1 ± 7.0	179.2 ± 8.7	-0.015 ± 0.026	0.053 ± 0.023
-8.31	1.8 ± 6.7	195.9 ± 7.7	0.008 ± 0.024	0.015 ± 0.022
-7.88	-0.1 ± 5.9	210.1 ± 7.6	-0.004 ± 0.022	0.041 ± 0.024
-7.44	6.3 ± 6.4	195.6 ± 8.0	0.014 ± 0.021	0.066 ± 0.024
-7.00	-7.2 ± 5.4	211.6 ± 8.1	-0.038 ± 0.020	0.034 ± 0.025
-6.64	0.2 ± 7.0	206.4 ± 8.2	-0.005 ± 0.023	0.043 ± 0.026
-6.05	-6.9 ± 6.1	194.4 ± 7.8	-0.006 ± 0.022	0.088 ± 0.022
-5.47	1.4 ± 6.4	209.6 ± 7.1	0.043 ± 0.019	0.034 ± 0.022
-5.18	5.7 ± 6.1	212.4 ± 7.7	-0.025 ± 0.019	0.076 ± 0.020
-4.59	7.8 ± 5.5	210.2 ± 7.1	0.006 ± 0.018	0.053 ± 0.019
-4.01	-3 ± 5.1	214.9 ± 6.7	0.038 ± 0.015	0.064 ± 0.019
-3.50	-0.1 ± 6.5	212.8 ± 8.0	-0.012 ± 0.017	0.065 ± 0.022
-3.06	-0.2 ± 5.9	228.9 ± 7.5	0.052 ± 0.016	0.041 ± 0.021
-2.04	-1.7 ± 4.8	218.8 ± 5.2	0.005 ± 0.014	0.062 ± 0.015
0.00	-0.2 ± 3.5	248.4 ± 4.0	0.026 ± 0.009	0.055 ± 0.011
1.02	2 ± 3.8	233.2 ± 4.4	-0.010 ± 0.012	0.051 ± 0.013
2.04	7.8 ± 5.3	226.7 ± 6.2	-0.009 ± 0.017	0.037 ± 0.015
3.07	-0.2 ± 6.2	226.4 ± 8.5	0.012 ± 0.022	0.080 ± 0.022
3.50	7.1 ± 7.5	215.7 ± 8.4	0.011 ± 0.025	0.065 ± 0.021
4.16	3.2 ± 6.5	210.7 ± 6.9	-0.001 ± 0.022	0.056 ± 0.020
4.45	0.9 ± 6.0	211.4 ± 7.8	-0.006 ± 0.023	0.036 ± 0.021
5.03	-1.5 ± 7.0	200.7 ± 8.5	0.000 ± 0.025	0.047 ± 0.026
5.62	1.0 ± 6.8	203.0 ± 8.2	0.004 ± 0.025	0.045 ± 0.023
5.91	4.4 ± 7.4	208.1 ± 8.5	-0.041 ± 0.026	0.060 ± 0.023
6.50	-5.5 ± 7.8	208.8 ± 8.7	-0.011 ± 0.028	0.007 ± 0.026
6.86	7.9 ± 6.7	198.1 ± 7.8	-0.005 ± 0.024	0.057 ± 0.022
7.73	-4.9 ± 6.7	193.1 ± 8.2	0.007 ± 0.027	0.023 ± 0.023
8.17	-12.8 ± 7.2	187.3 ± 9.0	-0.008 ± 0.028	0.055 ± 0.025
8.61	3.2 ± 7.3	197.6 ± 8.6	-0.020 ± 0.028	0.049 ± 0.022
9.12	-7.5 ± 6.6	188.5 ± 8.1	-0.028 ± 0.027	0.047 ± 0.023
9.70	0.5 ± 7.2	199.7 ± 8.5	-0.005 ± 0.026	0.033 ± 0.023
10.29	-13.4 ± 7.9	195.5 ± 9.0	0.032 ± 0.027	0.032 ± 0.023
10.94	-6.4 ± 7.0	181.9 ± 8.3	0.006 ± 0.028	0.059 ± 0.022
11.67	1.5 ± 8.2	186.3 ± 8.8	0.021 ± 0.029	0.056 ± 0.024
12.47	2.6 ± 7.2	195.1 ± 8.5	0.005 ± 0.028	0.058 ± 0.021
13.35	-5.0 ± 7.6	174.8 ± 9.2	-0.033 ± 0.029	0.071 ± 0.028
14.30	1.9 ± 7.9	185.3 ± 9.5	0.013 ± 0.029	0.036 ± 0.026
15.39	1.4 ± 7.8	191.2 ± 8.8	0.004 ± 0.029	0.010 ± 0.027
16.63	-5.9 ± 7.8	180.6 ± 8.4	0.037 ± 0.030	0.046 ± 0.023
18.01	-8.0 ± 7.2	188.6 ± 8.5	-0.006 ± 0.030	0.001 ± 0.026
19.62	1.3 ± 8.0	177.5 ± 7.9	-0.042 ± 0.031	-0.016 ± 0.025
21.44	-13 ± 7.4	172.8 ± 8.1	-0.003 ± 0.031	0.029 ± 0.024
23.48	-15.4 ± 7.3	155.6 ± 8.3	0.001 ± 0.031	0.022 ± 0.024
25.88	-6.2 ± 7.8	148.4 ± 7.8	-0.030 ± 0.032	0.053 ± 0.022
28.78	-2.8 ± 6.8	139.2 ± 7.8	-0.034 ± 0.029	0.083 ± 0.019
32.40	-21.1 ± 6.9	133.4 ± 8.1	0.068 ± 0.029	0.077 ± 0.020
37.30	-11.4 ± 7.0	146.9 ± 7.4	0.024 ± 0.031	-0.004 ± 0.025
44.70	-12 ± 6.8	143.4 ± 7.3	-0.001 ± 0.027	0.030 ± 0.017
58.08	-19.3 ± 6.6	116.7 ± 8.5	0.079 ± 0.017	-0.012 ± 0.012
97.33	-68.0 ± 8.1	109.6 ± 18.3	-0.009 ± 0.017	-0.025 ± 0.018

**Table 3.** Minor axis kinematics of NGC 7507.

$R$ (arcsec)	$v_{\text{rot}}$ (km s <sup>-1</sup> )	$\sigma_V$ (km s <sup>-1</sup> )	$h_3$	$h_4$
-81.02	-21.64 ± 26.2	133.5 ± 32.8	-0.021 ± 0.007	-0.004 ± 0.006
-46.29	25.06 ± 10.2	156.8 ± 11.5	-0.077 ± 0.019	0.003 ± 0.019
-34.90	22.56 ± 8.5	163.3 ± 10.1	0.008 ± 0.023	0.094 ± 0.018
-27.88	42.26 ± 8.0	159.9 ± 9.7	0.018 ± 0.023	0.129 ± 0.015
-16.66	34.56 ± 7.2	184.5 ± 9.5	0.017 ± 0.026	0.069 ± 0.024
-14.34	28.96 ± 7.2	173.6 ± 7.5	-0.016 ± 0.026	0.036 ± 0.022
-12.53	32.26 ± 7.1	193.2 ± 9.4	-0.004 ± 0.026	0.083 ± 0.022
-11.07	33.36 ± 7.5	196.5 ± 9.6	-0.064 ± 0.026	0.012 ± 0.028
-9.84	29.56 ± 7.2	185.9 ± 8.6	-0.046 ± 0.026	0.047 ± 0.025
-8.74	25.46 ± 6.3	184.5 ± 9.1	0.040 ± 0.025	0.055 ± 0.027
-7.80	19.86 ± 5.8	177.5 ± 8.4	0.021 ± 0.025	0.078 ± 0.024
-7.00	33.46 ± 6.1	188.8 ± 7.9	-0.036 ± 0.024	0.056 ± 0.022
-6.35	27.86 ± 7.2	194.4 ± 8.3	-0.040 ± 0.026	0.025 ± 0.025
-5.76	21.96 ± 6.3	201.5 ± 8.4	0.007 ± 0.025	0.031 ± 0.023
-5.18	18.76 ± 5.8	198.5 ± 7.5	-0.009 ± 0.024	0.046 ± 0.022
-4.67	15.76 ± 6.4	205.7 ± 8.9	0.011 ± 0.024	0.058 ± 0.026
-4.23	16.76 ± 5.9	211.4 ± 8.1	0.020 ± 0.022	0.030 ± 0.023
-3.79	20.16 ± 5.0	201.2 ± 8.0	0.029 ± 0.022	0.060 ± 0.022
-3.43	14.56 ± 6.0	204.1 ± 9.2	-0.007 ± 0.024	0.063 ± 0.025
-3.14	16.56 ± 6.1	210.7 ± 8.4	0.005 ± 0.022	0.046 ± 0.023
-2.04	1.26 ± 6.2	217.9 ± 8.8	0.035 ± 0.023	0.053 ± 0.022
-1.02	7.76 ± 4.8	227.4 ± 6.7	0.022 ± 0.017	0.064 ± 0.016
0.00	8.36 ± 4.0	245.4 ± 5.3	0.029 ± 0.012	0.078 ± 0.013
1.02	-11.04 ± 4.9	224.5 ± 5.3	0.034 ± 0.016	0.023 ± 0.019
2.11	-10.44 ± 4.3	212.1 ± 5.9	0.019 ± 0.015	0.067 ± 0.020
3.28	-20.44 ± 6.0	207.2 ± 7.1	-0.003 ± 0.020	0.019 ± 0.024
3.64	-26.94 ± 5.1	209.8 ± 6.9	0.029 ± 0.017	0.042 ± 0.020
4.08	-23.24 ± 6.4	212.7 ± 6.6	0.035 ± 0.019	0.030 ± 0.021
4.52	-23.14 ± 5.9	203.1 ± 6.6	-0.001 ± 0.020	0.021 ± 0.022
5.03	-33.94 ± 5.2	202.8 ± 6.4	0.013 ± 0.019	0.013 ± 0.023
5.62	-22.94 ± 6.9	189.9 ± 7.7	-0.043 ± 0.023	0.039 ± 0.026
6.27	-32.24 ± 6.5	183.9 ± 7.5	0.023 ± 0.023	0.062 ± 0.023
7.00	-30.14 ± 6.2	204.0 ± 7.4	-0.020 ± 0.022	0.021 ± 0.027
7.80	-36.94 ± 6.6	173.3 ± 7.3	0.014 ± 0.023	0.104 ± 0.021
8.74	-35.04 ± 6.2	187.7 ± 6.4	0.069 ± 0.023	0.023 ± 0.025
9.84	-54.44 ± 7.4	186.8 ± 7.0	0.079 ± 0.023	0.064 ± 0.024
11.14	-51.14 ± 7.6	179.9 ± 7.2	0.047 ± 0.024	0.069 ± 0.024
12.81	-43.04 ± 6.6	184.9 ± 7.9	0.018 ± 0.024	0.089 ± 0.025
14.92	-54.44 ± 6.6	174.4 ± 7.3	0.035 ± 0.025	0.056 ± 0.021
17.53	-61.14 ± 6.5	173.2 ± 7.7	0.033 ± 0.025	0.051 ± 0.025
20.87	-55.14 ± 7.5	179.3 ± 6.9	0.061 ± 0.025	0.015 ± 0.024
32.23	-54.74 ± 8.3	158.2 ± 8.3	0.047 ± 0.024	0.031 ± 0.023
42.16	-48.24 ± 7.5	122.1 ± 11.9	0.027 ± 0.014	0.034 ± 0.013
61.48	-8.44 ± 21.1	135.9 ± 27.4	-0.021 ± 0.009	-0.013 ± 0.007